國立交通大學

環境工程研究所

碩 士 論 文

鍛燒溫度對釩離子摻雜二氧化鈦光觸媒物化與光催化還原二氧化碳特性研究

The physicochemical properties and photocatalytic behavior of the

V-doped TiO$_2$ calcined at different temperatures for CO$_2$ reduction

研 究 生：林宸嶢

指導教授：張淑閔　副教授

中 華 民 國 一 百 年 八 月

致謝

　　大學畢業之後，有幸考上了交大環工所，並有幸的進入了環境奈米實驗室，因此開啟了我的碩士生涯；歷經了兩年的寒暑，我從青澀的大學畢業生，蛻變為能夠獨當一面的研究生，我能有這麼深遠的進步，一切都要歸功於我的指導教授 張淑閔老師，老師教導了我很多這領域的知識，並讓我能夠獨立思考，對自己的實驗進行規劃與研究，並培養了我認真、負責的態度，在此學生向老師致上最深的感謝。令承蒙清華大學董瑞安老師、台灣大學吳紀聖老師和同步輻射中心詹丁山博士，對於我的論文研究給予很多的建議與指導，讓我能夠完善我的論文實驗。

　　很高興能夠進來本實驗室，這裡就像一個大家庭一樣，有歡樂、有支持、有鼓勵、有互助，讓我的研究所生涯感到充實且歡欣。在此我要感謝精榮學長對於我實驗的指導，品欣學姊教導我儀器上的操作，姿吟學姊很有耐心的替我解開實驗上的疑惑，小 G 學姊嚴謹的指正我的錯誤，穎亞學長在二氧化碳還原上的指導與幫忙，少了你們這些親切又可靠的學長姐，就沒有今天的我；還有我的好同學 Ashley 跟 Jiphi，少了你們，實驗室就少了很多歡笑聲，我也少了很多支持的動力；還要感謝可愛又俏皮的學弟Jeremy，你的逗趣，讓我在這實驗室裡不會感到孤單與乏味；最後還要感謝我的家人，無怨無悔的支持著我，你們的鼓勵與愛護，讓我能夠全心全力的完成學業，你們是我最強大的後援，也是讓我努力的原動力，由衷的感謝你們，也很愛你們。

　　僅以本文獻給所以幫助我與關心我的大家。

<div align="right">

宸嶢 謹誌

中華民國 100 年 8 月

</div>

中文摘要

　　近年來，利用光觸媒進行光還原二氧化碳產生燃料之議題備受矚目，其中，有很多研究著重於參雜不純物至光觸媒二氧化鈦裡，藉由不純物減少電子電洞再結合的速率，有效提升二氧化鈦進行光還原二氧化碳的效率。本研究利用溶膠-凝膠法(sol-gel)製備摻雜釩離子的二氧化鈦，探討不同鍛燒溫度(200 °C-700 °C)與不同釩離子濃度(0.01 wt%與1.00 wt%)對二氧化鈦光觸媒結構以及光還原二氧化碳的影響。研究結果顯示 TiO_2 經 300 °C 鍛燒後呈現銳礦鈦的結構，鍛燒溫度超過 600 °C 會產生金紅石，而在 V/Ti 比例高於 1% 時，會使金紅石相在 500 °C 時，提早產生，另外，當鍛燒溫度高於塔曼溫度時，釩會往表面遷移而形成 V_2O_5 晶相，SIMS 實驗發現，高濃度釩在鍛燒 600 °C 時表面釩的濃度為鍛燒 200 °C 時的 7.6 倍，由 EPR 及 XAS 發現，在鍛燒溫度較低的樣品中，內部有三價與四價的釩參雜在二氧化鈦晶格中，而隨著鍛燒溫度增加，釩的價態會逐漸轉變為五價的型態，當鍛燒溫度增加到 600 °C，可由 GI-XRD 觀察到明顯的表面 V_2O_5 晶相產生，UV-VIS 光譜可發現參雜高濃度釩的樣品可明顯降低 TiO_2 能隙至 1.6 eV。在 300-500 °C 鍛燒溫度下，觸媒對 0.01 mM Rhodamine B 光降解活性依次為 0.01 at.% V-doped TiO_2> pure TiO_2 > 1.00 at.% V-doped TiO_2。在光還原二氧化碳的實驗裡，500 °C 鍛燒的樣品有最高還原活性，甲烷為還原反應中唯一可測得產物，單純 TiO_2 在反應第一小時有最高 CH_4 量子產率 2.98 %，其次為 1.00 at.% V-doped TiO_2 (2.65 %) 與 0.01at.% V-doped TiO_2 (2.44 %)，然而，於 8 小時反應後，各觸媒產生甲烷的量子產率依序為 1.00 at.% V-doped TiO_2 (0.66 %) >單純 TiO_2 (0.39 %)~0.01 at.% V-doped TiO_2 (0.39 %)。EPR 光譜發現，表面電荷於 CO_2 與 H_2O 分子間的轉移迅速，因此具低還原電位的中間產物是限制光催化還原效率的關鍵，表面缺陷造成傳導帶下低還原能力的能階決定釩摻雜二氧化鈦低初始還原活性，而 V_2O_5 與 TiO_2 間的異質界面則抑制甲烷再氧化速率。

Abstract

In this study, the physicochemical properties and photoreduction behavior of the TiO_2 samples doped with 0.01 and 1.00 at.% V ions and calined at different temperatures were investigated. The pure TiO_2 exhibited anatase phase at 300 °C and underwent phase transition to rutile one at 600 °C. Incorporation of V ions decreased the transition temperature to 500 °C. Calcination greatly increased the surface V/Ti ratio of the doped TiO_2 by 7.6 times as the temperature increased from 200 to 600 °C. The increase in the surface concentration of the V ions also led to the formation of V_2O_5 moiety. Doping 1.00 at.% V ions dereduced the bandgap energy of the TiO_2 from 3.1-3.3 to 1.6 eV. For oxidation of Rhodamine B, the photocatalysts exhibited the activity in the order of 0.01 at% V-doped TiO_2 > pure TiO_2 > 1.00 at. % V-doped TiO_2. The samples calcined at 500 °C showed the highest activity for CO_2 reduction over other temperatures. CH_4 was the only detectable product in the reduction systems. After 1 hr irradiation, the pure TiO_2 had the highest quantum efficiency (2.98 %) for CH_4 generation, followed by 1.00 at.% V-doped TiO_2 (2.65 %) and 0.01 at.% V-doped TiO_2 (2.44 %). However, the quantum efficiency of the photocatalysts for CH_4 yield after 8 hr irradiation was in the order of 1.00 at.% V-doped TiO_2 (0.66 %) > pureTiO_2 (0.39 %)~0.01 at.% V-doped TiO_2 (0.39 %). The EPR results showed that interfacial charge transfer from the photocatalysts to the adsorbed CO_2 and H_2O is efficient. Thus, the reduced intermediates determined the low reduction efficiency of CO_2 to CH_4. The impurity levels locating below the conduction band result in slow reduction kinetics., and the presence of V_2O_5 moiety at the surface inhibited the reoxidation of CH_4.

Index

Table Index

Figure Index

Chapter 1. Introduction

1-1 Motivation

In the last century, the industrial development and energy needed caused people widely used the fossil fuels in power plants and transportation.   Unfortunately, the burning of fossil fuels will be accompanied by carbon dioxide emissions.   Recently, using sunlight to directly converse of CO_2 and water vapor into fuels by photocatalysts has been considerable concerned.[1] TiO_2 (Titanium dioxide) is the widely use for decomposition of environmental pollutants because it is cheap, highly chemical stable and nontoxic characteristics.[2]   To enhance its photocatalytic activity, impurities including transition metal ions including Cr, V, Mn, Fe, or Co were doped into the TiO_2 lattice to modify its electronic structures and microstructures.[3-5]   The benefits of the modification of the photocatalytic activity include (1) to increase the wavelength response range; (2) the inhibition of recombination by increasing the charge separation; and (3) change in the selectivity or yield of a particular product.

Many researchers focused on the photoreduction of CO_2 by metal-modify TiO_2.   Wu *et al*.[6] coated Ag-TiO_2 and Cu-TiO_2, respectively, on the optical fiber and Vapor-phase CO_2 was photocatalytically reduced to methanol.   Wang *et al*.[7] shows that CdSe quantum dot (QD)-sensitized TiO_2 heterostructures are capable of catalyzing the photoreduction of CO_2 using visible light illumination ($\lambda > 420$ nm). Some studies indicate that doping some metal ions can increase CO_2 adsorption.   Adachi *et al*.[8] reported the Cu-TiO_2 powders suspended in the solution reduce CO_2 and yield 21.8 μl/g, 26.2 μl/g, and 2.7 μl/g methane, ethylene, and ethane, respectively.

Vanadium ions are one of the most interesting dopants which make TiO_2 visible. Klosek[3] reported that vanadium-doped TiO_2 extended the wavelength range of the catalyst

1

into 365-450 nm and highly improved the photocatalytic activity of TiO_2 under solar light irradiation. Choi *et al*.[9] showed that V^{4+} in TiO_2 lattices effectively decreased the electron-hole recombination. Wachs *et al*.[10] reported that V_2O_5 crystals were observed on the surface of TiO_2 when the temperature was higher than its Tammann temperature. The p-n junction between the V_2O_5 and TiO_2 promoted the photocatalytic activity. Bronkema *et al*. [11] showed that CO_2 adsorbed on V-TiO_2 is higher than pure TiO_2. It means that there is more efficiency of photoreduced CO_2. However, the physicochemical and photocatalytic properties of photoreduction of CO_2 by vanadium ions doped TiO_2 have not been documented yet.

1-2 Objectives

In this study, we aim to investigate the effects of V-doped TiO_2 on photoreduction of CO_2 to hydrocarbon fuel in the gas phase. The doped materials were prepared by sol-gel method. We will find out the best ability to promote the photoreduction of vanadium doping concentration, calcination temperature, the mechanism and physicochemical properties of photoreduction of CO_2 by V-doped TiO_2.

.

Chapter 2. Background and Theory

2-1 Photocatalysis and Photocatalysts

2-1-1 TiO_2 photocatalysts

In 1972, photocatalysis of TiO_2 nanoparticles has been found that can be used for degrading pollutions in water or air.   Afterward, many investigations have been carried out with the aim of enhancing photocatalytic efficiencies of the process.   In order to improve the efficiency of photoactivity, impurities including transition metal ions including Cr, V, Mn, Fe, or Co were doped into the TiO_2 lattice to modify its electronic structures and microstructures. [3-5, 12]   Nowadays, TiO_2 has been widely used in industrial application such as solar energy cell[13], photocatalysis[14], gas sensors[15] and CO_2 photoreduction.[16]

The energy difference between the energies of the valence band and the conduction band of electron energy in semiconductors is called the band gap.   Generally, semiconductor can be excited by energy in terms of photon energy, *hv*.   A photon will excite an electron from the valence band to the conduction band, thereby the excited semiconductor has electrons and holes pairs for further redox reactions.[17-19]   This process also shows in Figure 2-1.

When the heterogeneous photocatalyst absorbs UV energy which is higher or equal to the band gap energy of semiconductors, it will generate the electron-hole pair (e^--h^+ pair). While several situations of the electron-hole pair may occur.   The electron-hole pair can recombine in the bulk or on the surface of the particle in a few nanoseconds.   The electron-hole pair can migrate to the photocatalyst surface and then be trapped in surface states.   The electron-hole pair trapped in surface states can proceed the redox reaction with the compounds adsorbed on the catalyst.   Figure 2-2 shows the basic electron transitions in an activated semiconductor.
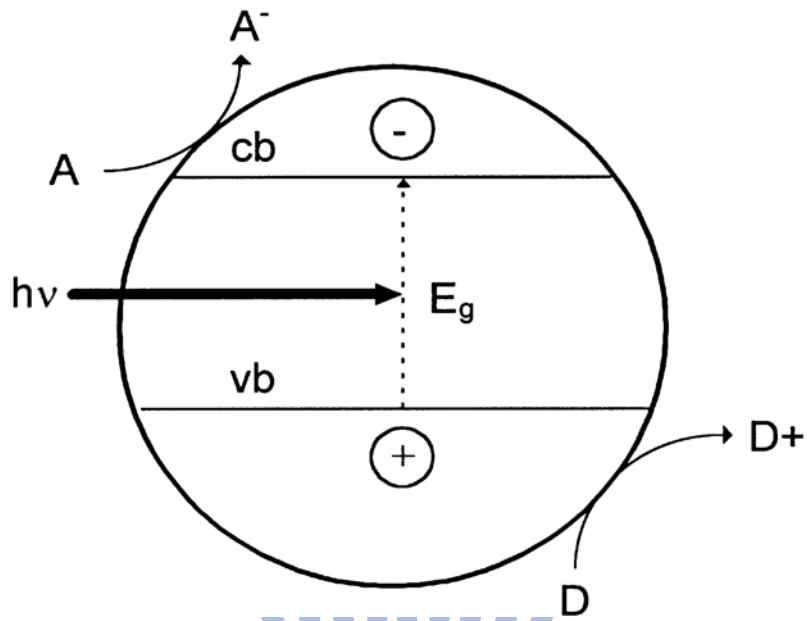
Figure 2-1 Simplified diagram of the photocatalytic processes occurring on an illuminated semiconductors.[20]
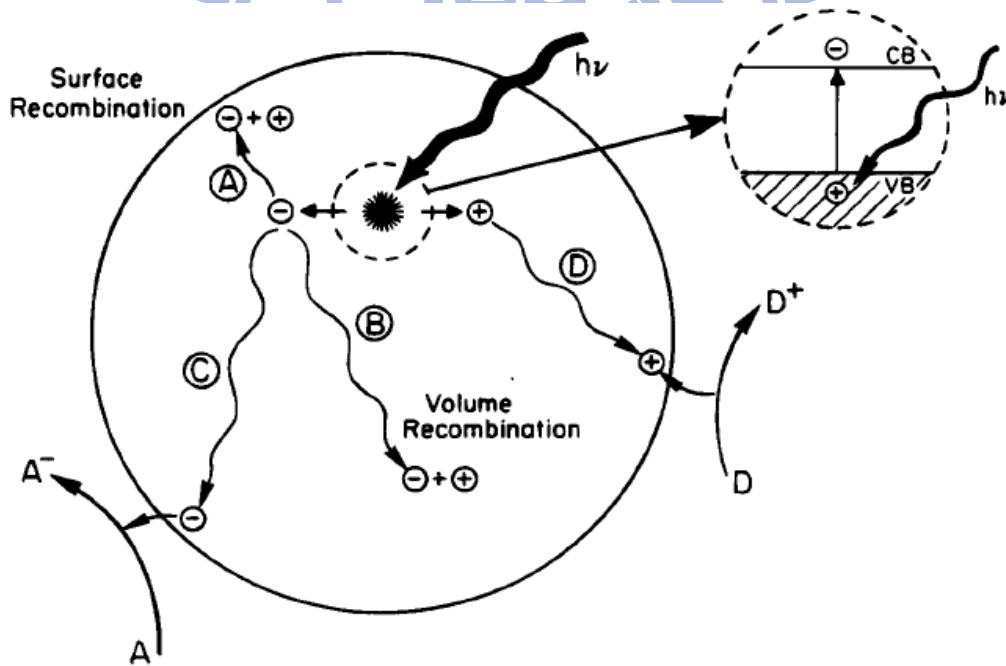
Figure 2-2 Schematic photoexcitation in a solid followed by deexcitation events.[17]

Thermodynamically, the adsorbed pollutants can be photoreduced by conduction band (CB) electrons if they have redox potentials more positive than the flatband potential of the CB. Also, they can be oxidized by holes in the valence band (VB) if they have redox potentials more negative than the flatband potential of the VB. The proposed mechanisms can be expressed by the following set of simplified equations step by step.[20]

Step I: Band gap illumination (hv) onto a photocatalyst causes the electronic transitions.

$$TiO_2 \xrightarrow{\quad hv \quad} e^- + h^+$$
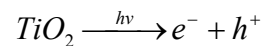
Step II: Organic molecule adsorbed on the catalyst surface and lattice oxygen (O_L^{2-}).

$$O_L^{2-} + Ti^{IV} \rightarrow O_L H^- + Ti^{IV} - OH^-$$
$$Ti^{IV} + H_2O \rightarrow Ti^{IV} - OH^-$$
$$Site + R_1 \rightarrow R_{1ads}$$
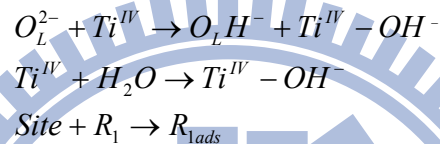
where R_1 represents an organic molecule, R_{1ads} represents an adsorbed organic molecule

Step III: Photogenerated holes oxidize the adsorbed OH⁻ and water and electrons react with adsorbed O_2.

$$Ti^{IV} - OH^- + h^+ \rightarrow Ti^{IV} - OH^\bullet$$
$$Ti^{IV} - H_2O + h^+ \rightarrow Ti^{IV} - OH^\bullet + H^+$$
$$R_{1ads} + h^+ \rightarrow R_{1ads+}$$
$$Ti^{IV} + e^- \rightarrow Ti^{III}$$
$$Ti^{III} + O_2 \rightarrow Ti^{IV} - O_2^{\bullet-}$$
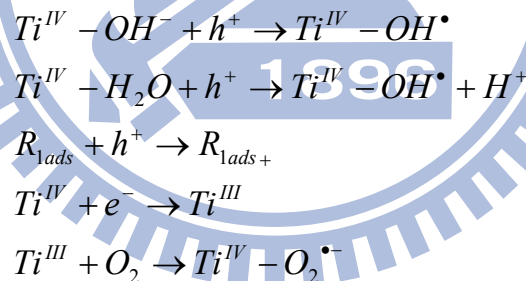
The free radicals attack the organic molecule under different conditions:

Case I $\quad Ti^{IV} - OH^\bullet + R_{1ads} \rightarrow Ti^{IV} + R_{2ads}$

Case II $\quad OH^\bullet + R_{1ads} \rightarrow R_{2ads}$

Case III $\quad Ti^{IV} - OH^\bullet + R_1 \rightarrow Ti^{IV} + R_2$

Case IV $\quad OH^\bullet + R_1 \rightarrow R_2$
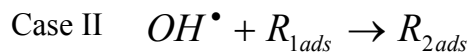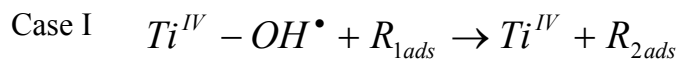
In recent years, numerous photocatalyst materials, such as TiO_2, ZnO, ZnS, SnO_2 and CdS, have been widely discussed and applied in dealing with water pollution or air pollution.

Figure 2-3 shows the redox potentials of various semiconductors. The titanium dioxide has been attracting more attention due to its non-toxicity, chamical stability, high photocatalytic activity, optical properties, low cost and suitable band gap energy.[21, 22]

TiO$_2$ has two polymorphs: anatase and rutile. Figure 2-4 shows the crystalline structures of the anatase and rutile TiO$_2$. Each Ti^{4+} ion is surrounded by an octahedron of six O^{2-} ions. In the anatase structure, each octahedron contacts with 8 neighboring octahedrons, while in the rutile structure each octahedron contacts with 10 neighbors. The metastability of the anatase phase can transfer leads phase transformation to the rutile phase when calcination temperature is higher than 550 °C. The band gap of anatase and rutile are 3.2 eV and 3.0, respectively. Generally, anatase shows higher adsorptive ability and lower rate of charge recombination than rutile.[14]
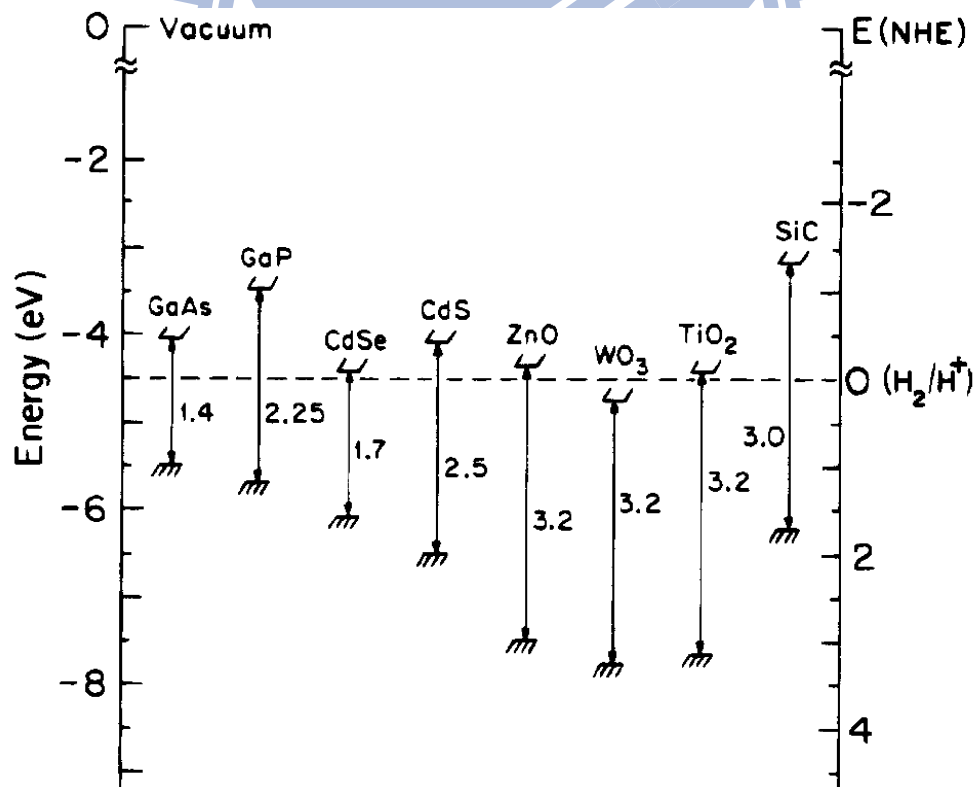
Figure 2-3 The band edge position of various semiconductors.[17]

6
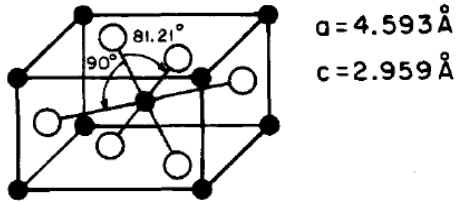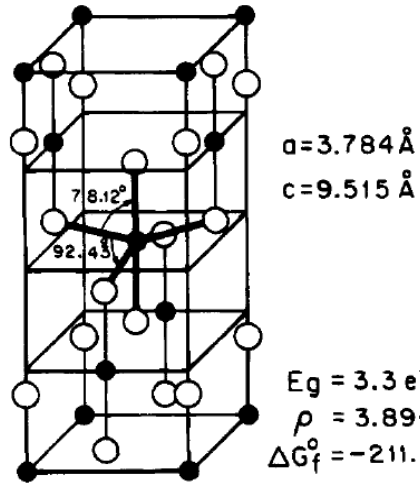
Figure 2-4 Structure of rutile and anatase TiO_2.[17]
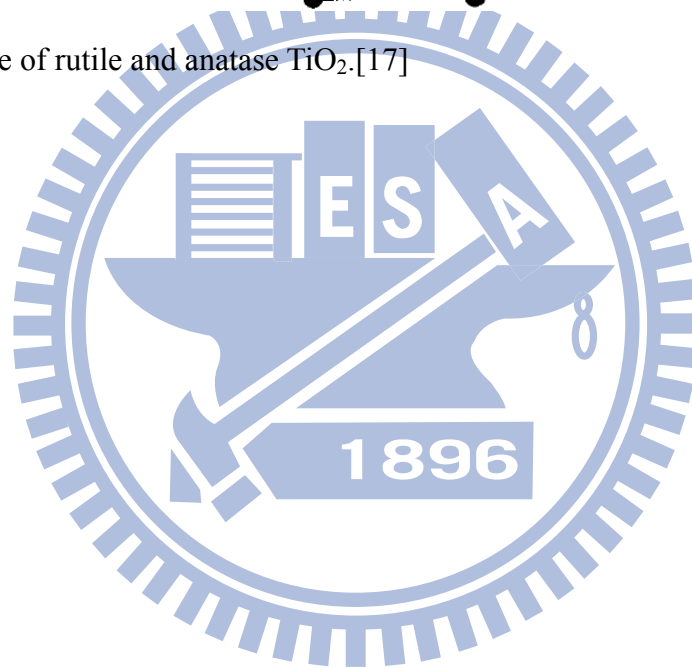
2-1-2 Modified TiO$_2$ photocatalysts

Photocatalytic activity of a particular semiconductor system for the stated purpose was measured by some factors like the efficiency of the photocatalytic process, the stability of the semiconductor under illumination, the wavelength range response, and the selectivity of the products. Therefore, the limitations of a particular semiconductor as a photocatalyst for a particular use can be overcomed by modifying the semiconductor. There are three benefits of modifications to photocatalytic semiconductor systems: (1) inhibiting e$^-$-h$^+$ recombination by increasing the charge separation and increasing the efficiency of the photocatalytic process; (2) increasing the wavelength response range and (3) changing the selectivity or yield of a particular product.

The typical modifications include doping transition metal ions (Cr, V, Fe)[3-5] or non metal ions (C, N)[23, 24] into TiO$_2$ lattice and combining TiO$_2$ with another semisonductor (CdSe)[7]. The modifications change the microstructures and electronic structures, so that alter the physicochemical properties and photocatalytic acitivity. Among those researches, doping vanadium seems to be an effective route in the theoretical viewpoint. Zhao *et al*. and Wu *et al*. [25, 26] found that V-doped TiO$_2$ resulted in a red shift of the absorption band edge. Anpo *et al*. [27] modified TiO$_2$ catalysts by bombarding V, Cr, Mn, Ni, or Fe, respectively, with high-energy metal ions. The metal ion-implanted TiO$_2$ showed the V ions had the highest effectiveness in the red shift. Table 2-1 lists some important literatures of TiO$_2$ and V-doped TiO$_2$.

Table 2-1 The development of titanium dioxide.

Year	Authors	The results and findings	Ref.
1972	Fujishima *et al*.	First developed electrochemical photolysis of water at a semiconductor electrode.	[28]
1992	Davidson *et al*.	Investigated temperature-induced diffusion V ions into the TiO_2 by ESR techniques	[29]
1994	Choi *et al*.	Summarized metal-ion dopants in quantum-sized TiO_2	[9]
1995	Linsebigler *et al*.	Summarized the mechanisms of photocatalysis of TiO_2	[17]
1999	Litter *et al*.	The mechanisms of photocatalysis of metal ions doped in TiO_2	[20]
1999	Zhao *et al*.	Sol-gel preparation of $Ti_{1-x}V_xO_2$ solid solution film electrodes with conspicuous photoresponse in the visible region	[25]
2001	Rodella *et al*.	Chemical and structural characterization of V_2O_5/TiO_2 catalysts	[30]
2002	Zhao *et al*.	Photoelectrochemical properties of sol-gel-derived $Ti_{1-x}V_xO_2$	[31]
2004	Wu *et al*.	A visible-light response vanadium-doped titania nanocatalyst by sol–gel method	[26]
2005	Anpo *et al*.	The preparation and characterization of highly efficient titanium oxide-based photofunctional materials	[27]
2006	Kemp *et al*.	Characterisation of transition metal-doped TiO_2	[4]
2007	Bouras *et al*.	The structural of pure and metal-ion-doped nanocrystalline titania for photocatalysis	[5]
2008	Izumi *et al*.	Photo-oxidation over mesoporous V-TiO_2 catalyst under visible light monitored by vanadium K $\beta_{5,2}$-selecting XANES spectroscopy	[32]
2010	Xu *et al*.	Photocatalytic activity of vanadium-doped titania-activated carbon composite film under visible light	[33]
2010	Hoffmann *et al*.	Combinatorial doping of TiO_2 with platinum (Pt), chromium (Cr), vanadium (V), and nickel (Ni) to achieve enhanced photocatalytic activity with visible light irradiation	[34]
2011	Chang *et al*.	Surface doping is more beneficial than bulk doping to the photocatalytic activity of vanadium-doped TiO_2	[35]

2-2 V-doped TiO$_2$ photocatalyst

2-2-1 Physicochemical properties of V/TiO$_2$

Transition metal doping can change the physicochemical properties of TiO$_2$. In order to understand the structure of vanadium in titanium dioxide, FT-Raman can help us to understand the structure of the vanadium doped TiO$_2$ catalysts. Figure 2-5 and Figure 2-6 show the structure of bulk and surface doped materials. There are two forms of VO$_X$ species attached to the TiO$_2$ surface for surface doped materials: monomeric vanadyl and polymeric vanadates.[30, 36, 37] In addition, the potentially active oxygen sites proposed to be interface V-O-Ti, surface Ti-O-Ti (638 cm^{-1}), bridging V-O-V(822 cm^{-1}), and vanadyl V=O (1030 cm^{-1}). When the number of vanadium in the polyvanadates increase, the number of terminal V=O (930 cm^{-1}) decreases and forms the number of accommodate V-O-V (822 cm^{-1}) linkages.[30, 36, 37] It shows that the vanadium ions are preferred to perform V$_2$O$_5$ under higher vanadium concentration. The doped vanadium ions diffused to the sample surface and formed V$_2$O$_5$ crystals when the calcination temperature was higher than their Tammann temperature(i.e. 209°C).[29, 38]
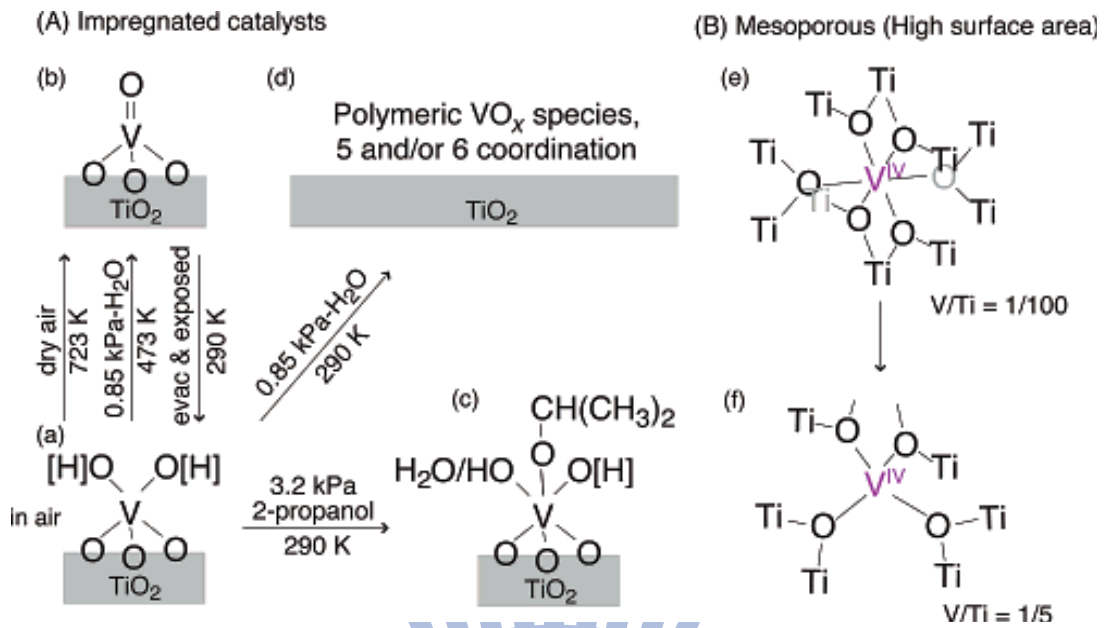
Figure 2-5 Proposed V site transformations for V/TiO$_2$ in reactant/product gas (A) and for mesoporous V-TiO$_2$ by changing the molar ratio of V/Ti (B).[H for models a and c indicates the presence/absence of hydrogen cannot be determined.[37]
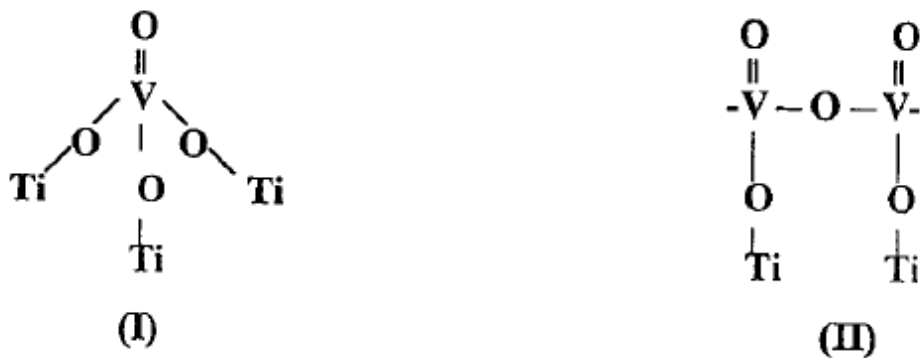
Figure 2-6 The structure of vanadium attached to the TiO$_2$ surface.[39]

2-2-2 Photocatalytic behavior of V/TiO_2

When doping the impurity into TiO_2, the defect can trap an electron or a hole alone and decrease the recombination time. Generally, The photochemical mechanisms, including charge recombination, charge-trapping, and migration mechanism, in the existence of transition metal ion dopants is showed as Figure 2-7 where M^{n+} is a metal ion dopant, R is an electron donor, and O is an electron acceptor:

charge pair generation   recombination

$$TiO_2 + h\nu \rightarrow e_{cb}^- + h_{vb}^+$$

$$e_{cb}^- + h_{vb}^+ \rightarrow TiO_2$$

$$M^{n+} + h\nu \rightarrow M^{(n+1)+} + e_{cb}^-$$

$$Ti^{3+} + >OH^\bullet \rightarrow Ti^{4+} + >OH^-$$

$$M^{n+} + h\nu \rightarrow M^{(n-1)+} + h_{vb}^+$$

$$M^{(n-1)+} + h_{vb}^+ \rightarrow M^{n+}$$

charge trapping

$$M^{(n-1)+} + >OH^\bullet \rightarrow M^{n+}$$

$$Ti^{4+} + e_{cb}^- \rightarrow Ti^{3+}$$

$$M^{(n+1)+} + e_{cb}^- \rightarrow M^{n+}$$

$$M^{n+} + e_{cb}^- \rightarrow M^{(n-1)+}$$

$$M^{(n+1)+} + Ti^{3+} \rightarrow M^{n+}$$

$$M^{n+} + h_{vb}^+ \rightarrow M^{(n+1)+}$$

interfacial charge transfer

$$>OH^- + h_{vb}^+ \rightarrow >OH^\bullet$$

$$e_{cb}^- (or\ Ti^{3+}, M^{(n-1)+}) + O \rightarrow O^-$$
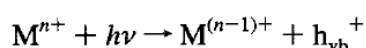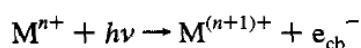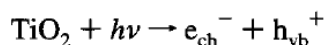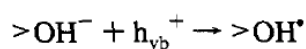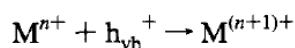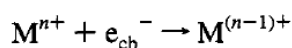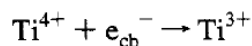
charge release and migration

$$h_{vb}^+ (or >OH^\bullet, M^{(n+1)+}) + R \rightarrow R^+$$

$$M^{(n-1)+} + Ti^{4+} \rightarrow M^{n+} + Ti^{3+}$$

$$M^{(n+1)+} + >OH^- \rightarrow M^{n+} + >OH^\bullet$$
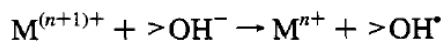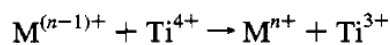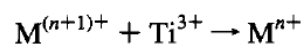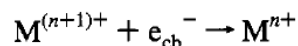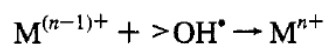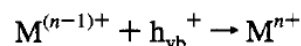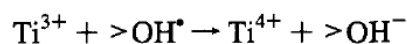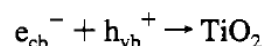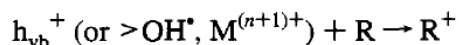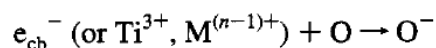
Figure 2-7 The photochemical mechanism in the present of transition metal ions.[9]

The addition of moderate transition metals into TiO_2 can increases the rate of photocatalytic oxidation, because the electron scavenges by the transition metal ions at surface through the following reaction: $M^{n+} + e_{cb}^- \rightarrow M^{(n-1)+}$. The transition metal ions prevent electron-hole recombination and result in an increase rate of formation of $OH^\bullet$

radical. In addition, the valence of the transition metal ions can also affect charge trapping. If the dopants act as holes trapping and electrons trapping, it can decrease the rate of recombination. For example, V^{4+} can act as both an electron trap and a hole trap in TiO_2 lattice. Thus, the photoactivity of V^{4+} is significantly higher than that of V^{5+} since V^{5+} can only trap electrons.[9]
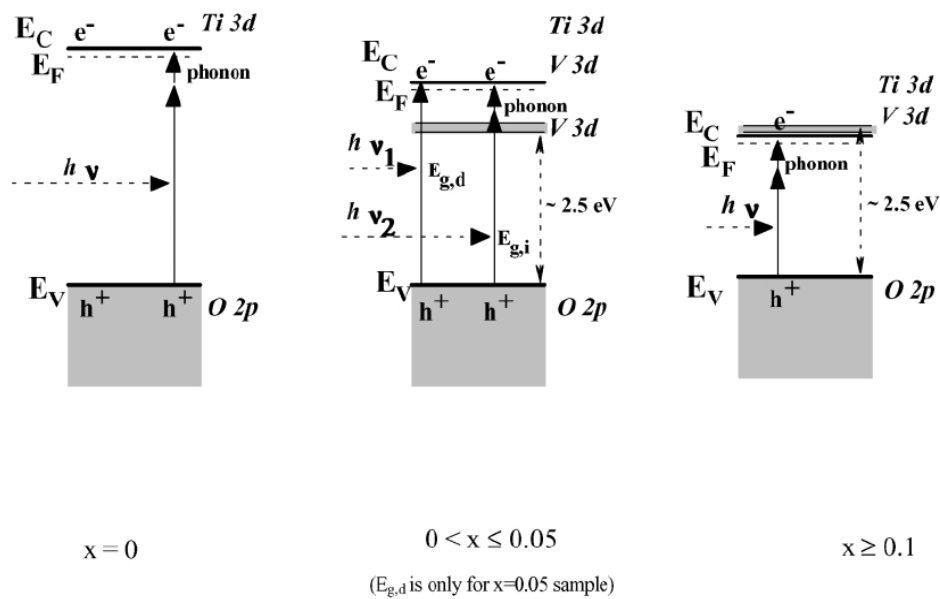
Figure 2-8 Band model of $Ti_{1-x}V_xO_2$ film electrodes at bias potential in an electrolyte solution.[31]

Besides, the atomic ratio of V/Ti can affect the electronic structure. Figure 2-8 shows the band model of $Ti_{1-x}V_xO_2$ at bias potential at various atomic ratio of V/Ti. The filled V 3d level acted as a donor level in the band gap. For V/Ti between 0 and 0.05 samples, the recombination time was longer than without V sample. That is because the V 3d level in the band gap inhibited the electron-hole recombination. However, when the amount of the V increased (V/Ti≧0.1), the donor level may connect with the conduction band. The crystals may shorten the distance between the V 3d level and the top of the valence band. Summary, changing the atomic ratio of V/Ti affect the electronic structure of materials.[31]

2-3 Photoreduction of CO_2

2-3-1 Reduction behavior

Fossil fuels are the most important source of energy in the world because of their stability and high energy density ($33GJ/m^3$ for gasoline). Unfortunately, Due to mass consumption of fossil fuels, it could release a large amount of CO_2 which is a kind of greenhouse gas. Many researchers suggest that the average global temperature will increase by about 6 °C in the end of this century. Hansen *et al.* used paleoclimate data to find out that an average global temperature change of 6 °C can lead to melting the ice in Antarctica and Rising sea levels.[40] Therefore, fossil fuels depletion and global warming have become the urgent environmental problems in the world.

In order to reduce the amount of CO_2, scientists use a lot of methods to collect CO_2 or convert CO_2 into hydrocarbon fuels. Biomass to fuel conversion shows the most promising way to biofuel production. Chisti *et al.* [41] shows that the microalgae have a oil content of more than 30%. Unfortunately, microalgae has some drawbacks: the energy conversion efficiency of photosynthesis is only approximately 1% and the microalgae required great land and water areas. Thermochemical has been used in converting CO_2 into CO. Galvez *et al.* and Bamberger *et al.*[42, 43] use Zn/ZnO cycle and CeO_2, respectively, to reduce CO_2 to CO. However, a number of materials challenges associated with large energy requirement in the reaction need to be solved for its development.

Using solar energy to convert CO_2 and water vapor into hydrocarbon fuels by photocatalysts become an attractive prospect. Be able to reduce carbon dioxide by using the photocatalysts, the conduction band of photocatalyst must be higher than the reduction potential of CO_2. The excited electronic from the conduction band can be transferred to CO_2 and then reduced CO_2. Inoue et al.[44] suggested that conversion of CO_2 to methane was given by

$$H_2O + 2h^+ \rightarrow \frac{1}{2}O_2 + H^+$$
$$CO_{2(aq)} + 2H^+ + 2e^- \rightarrow HCOOH$$
$$HCOOH + 2H^+ + 2e^- \rightarrow HCHO + H_2O$$
$$HCHO + 2H^+ + 2e^- \rightarrow CH_3OH$$
$$CH_3OH + 2H^+ + 2e^- \rightarrow CH_4 + H_2O$$
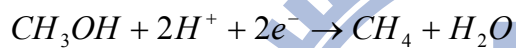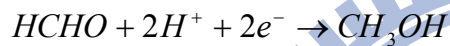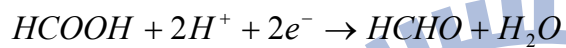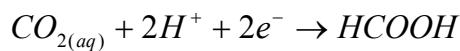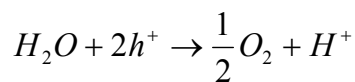
which e^- and h^+ mean photogenerated electrons and holes, respectively. Figure 2-9 shows the bandedge positions of the different semiconductor materials and redox potentials of the different chemical species. If the conduction band edge lies at a higher position than the redox potential, that is believed to be responsible for the high rates of product formation. The reaction also need a hole-scavengers to inhibit the recombination of hole–electron pairs. Scientific studies on photoreduction of CO_2 by semiconductor are listed in Table 2-2.
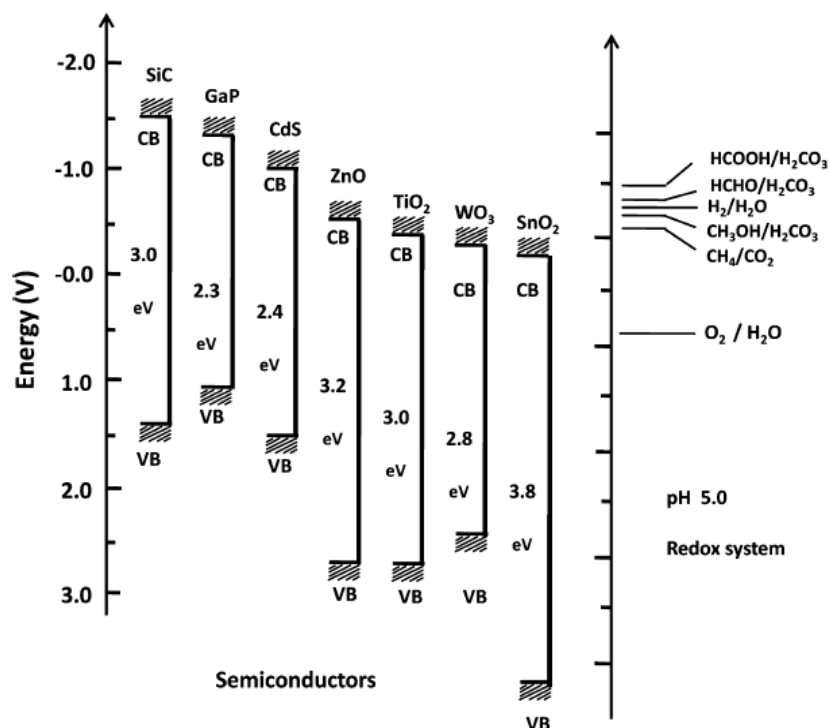
Figure 2-9 The bandedge positions of the different semiconductor materials and redox potentials of the different chemical species.

Table 2-2 Summary of some important reports on photoreduction of CO_2.

Catalyst	Light source	medium	products	Ref.
p-GaP crystal	Hg lamp	CO_2-saturated buffered solution	Methanol, formic acid, formaldehyde	[45]
Cu-TiO$_2$	UV lamp	Aqueous suspension	Methane, ethylene	[8]
TiO$_2$ on zeolite	UV lamp	H$_2$O vapor	Methanol	[46]
Cu-ZnO$_2$	UV lamp	NaHCO$_3$ solution	CO	[47]
P25, TiO$_2$	UV lamp	H$_2$ and H$_2$O	CO, methane, methanol	[48]
Ag/Cu-TiO$_2$	UV 365 nm	H$_2$O vapor	Methanol	[6]
CdSe/Pt/TiO$_2$	vis 420 nm	H$_2$O vapor	methane	[7]

2-3-2 Reaction mechanism in liquid phase

Some reseachers focus on the CO_2 reduction by photocatalysts in the liquid phase. Halmann *et al.* used the $SrTiO_3$ catalyst powder suspended in a liquid phase through which CO_2 was bubbled, to produce formic acid, formaldehyde, and methanol by natural sunlight.[49]   Sayama *et al.* reported that use of 1% Cu-loaded ZrO_2 catalyst for photocatalytic reduction of CO_2 to produced CO in $NaHCO_3$ solutions under UV irradiation.[47]   Tseng *et al.* used Cu-loaded titania to photoreduce CO_2 to produce methanol.   The methanol yield was Greatly increased by adding NaOH because NaOH in liquid could act as strong hole-scavengers, form OH radicals and enhance the solubility of CO_2.[50]   Pressure is also a very important parameter on photocatalytic reduction of CO_2 in solutions.   Takayuki showed that the optimum value of CO_2 pressure on photoreduction can produce the highest methanol.[51]   In summary, adjusted some important Parameters in photoreaction of solution phase, like the solubility, the optimum value of CO_2, and high active hole-scavengers, can increase the photoreduction of CO_2 to produce hydrocarbon fuels.

2-3-3 Reaction mechanism in gas phase

In recent years, more and more attention has been focus on the photocatalytic reduction of gaseous CO_2.   The general selection of hole-scavengers are H_2 gas or water vapor.   The photoactivity of CO_2 reduction are effective by H_2.   Lo *et al.*[48] reduced CO_2 with H_2 and H_2O to produce methane, ethane and CO.   But hydrogen is artificial production which need Additionally input the energy.   Therefore, a lot of researchers focus on the photoreduction of CO_2 with H_2O.   Wang *et al.*[7] shows that CdSe quantum dot (QD)-sensitized TiO_2 heterostructures are capable of catalyzing the photoreduction of CO_2 using visible light illumination ($\lambda > 420$ nm) in the presence of H_2O. However, carbon dioxide and water vapor

are competitive adsorptions. In Figure 2-10, Anpo *et al.*[46] showed the reaction mechanism of the photoreduction of CO_2 with H_2O on the anchored titanium oxide catalyst. H_2O and CO_2 molecules interacted with the excited state of photoinduced $(Ti^{3+}-O^-)^*$ species, the decomposition of H_2O and the reduction of CO_2 proceed competitively, depending on the ratio of CO_2 to H_2O. These interactions resulted in the formation of OH radicals, H atoms and carbon species, and these intermediate radical species react with each other to form CH_4 and CH_3OH. In summary, the choice of hydrogen and water vapor to be the hole-scavenger can effect the mechanism of photoreduction of CO_2. The ratio of CO_2 to H_2O must be considered because it will affect the yield of products and variety of products.
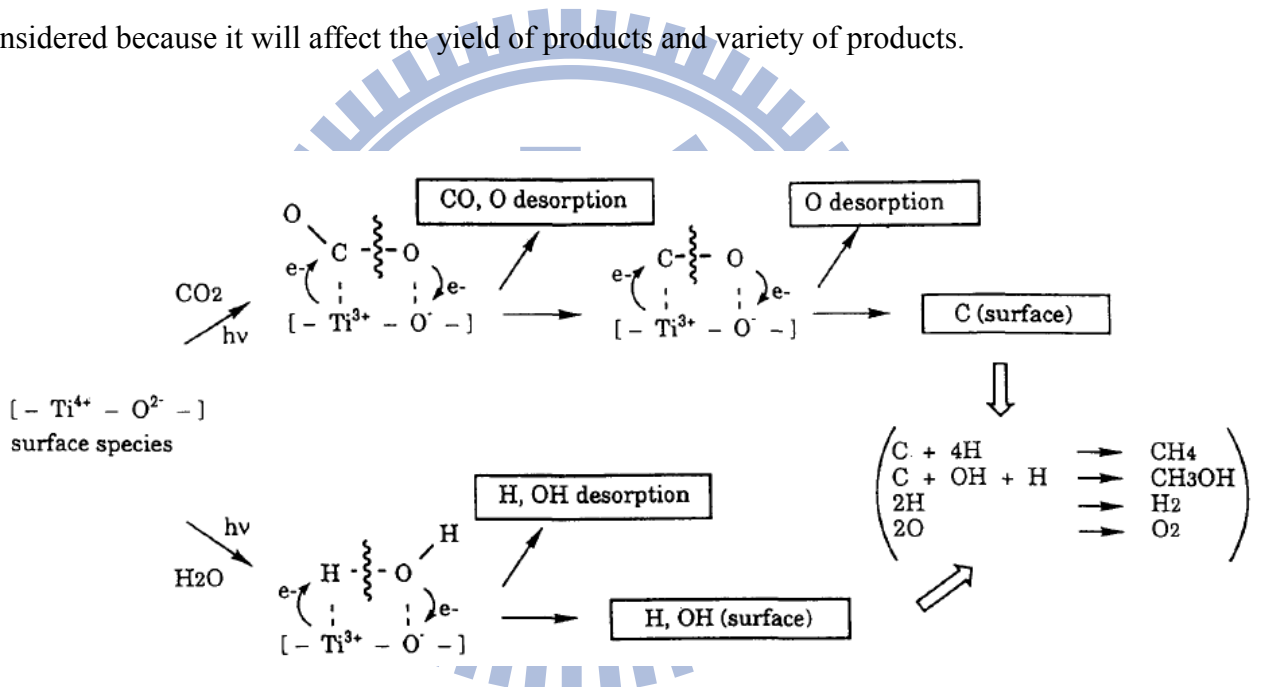
Figure 2-10 The photocatalytic reduction of CO_2 with H_2O on the titanium oxide.

Chapter 3. Materials and Methods

3-1 Materials

The precursors of titania and vanadium were titanium isopropoxide (TTIP, Acros, 98 %+) and vanadium (V) oxytriisopropoxide (VTIP, Aldrich, 99 %+), respectively.   2-propanol (C_3H_7OH, J.Backer, 100 %) was used as solvent to dissolve the precursors.   Rohdamine B (RhB, $C_{28}H_{31}N_2O_3Cl$, Sigma Aldrich, Dye content 95 %) was used to test the activities of the photocatalysts.   Hydrogen acid (HCl, Crown, 35~37 %) was used to adjust the pH values of the hydrolyzed sol solution.

3-2 Preparation of vanadium doped TiO$_2$ using a sol-gel method

In the beginning, VTIP and TTIP were dissolved in 70 mL isopropanol to obtain the V/Ti atomic ratios of 1×10^{-4} and 1×10^{-2}.   Afterward, 2 mL hydrochloric acid (24.5%, HCl) was injected into mixed solution at 4°C with stirring at 250 rpm for 9 hours to complete the hydrolysis of the VTIP and TTIP.   Then, the solutions underwent gelation at ambient temperature for 4 hours.   The doped TiO$_2$ powders were obtained after solvent was evaporated at 100°C for 2 days followed by 150°C for 3 hours.   The powders were then calcined under air at various temperatures (200~ 700°C).

3-3 Characterization

3-3-1 Specific surface area

TriStar 3000 gas adsorption analyzer was used to measure the BET (Brunauer, Emmett, and Teller) surface area of catalysts by N_2 physisorption.   The surface area of the samples was estimated according to the N_2 adsorption data by the BET model.   Before the N_2 adsorption, the sample was dried at 90 °C for 3 h and degassed at 120 °C for 6 h.

3-3-2 UV/Vis diffuse reflectance spectroscopy (UV/Vis-DRS)

The wavelength response range of the samples was recorded using an UV-vis spectrometer (HITACHI U-3010).   The Al_2O_3 was used to be the reference.   The spectra were recorded from 700 to 200 nm at a scanning rate of 300 nm/min.   The bandgap of samples can be calculated by transformed the spectra into absorption according to Kubelka-Munk equation.[52]

$$F(R) = \frac{(1-R)^2}{2R} = \frac{k}{S}$$ (3-1)

k is an absorption coefficient, S is a scattering coefficient, and R is reflectance.

3-3-3 Time-of-Flight Secondary Ion Mass Spectrometer (ToF-SIMS)

ToF-SIMS (ION-TOF, Munich, Germany) was used to analyze the surface composition of the sample. The primary ion source was a pulsed Ga^+ source operated at 25 keV. The sputter time was 120 s. The pressure of the main chamber was around 10^{-9} mbar. The surface atomic ratio was calculated by sub-equation

$$\rho_i = \frac{I_i}{I_m} RSF \qquad\qquad (3\text{-}2)$$

Where RSF (relative sensitivity factor) is the conversion factor from secondary ion intensity to atom density, the unit of RSF is atoms/cm^3, ρ_i is the impurity atom density in atoms/cm^3, I_m is the matrix isotope (Ti, m/z= 50.8) secondary ion intensity in counts/s and I_i is the impurity isotope (V, m/z= 47.9) secondary ion intensity in counts/s.

3-3-4 Inductively Coupled Plasma Mass Spectrometry (ICP-MS)

Bulk chemical compositions for V/Ti weight ratio was analyzed by Inductively coupled plasma mass spectrometry (ICP-MS, Perkin Elmer, SCIEX ELAN 5000). It is based on coupling together an inductively coupled plasma as a method of producing ions (ionization) with a mass spectrometer. All the samples were digested with acid solution coupled with microwave.

3-3-5 X-ray diffractometry

The X-ray powder diffractometer (XRPD, MAC Sience, MXP18) was used to examined the crystal structure and grain size by using the CuKα radiation (λ= 0.15405 nm) and the operating conditions are at an accelerating voltage of 30 kV and an emission current of 20 mA.   The range of the scanning 2θ is from 15° to 80° at sample width of 0.02° and scanning speed is 4°/min. The crystalline size (D) of all samples was estimated from Scherrer's equation:[53]

$$D = \frac{K \times \lambda}{\beta \times \cos\theta} \tag{3-3}$$

Where λ is the x-ray wavelength (Cu Kα= 0.15406 nm), β is the width of the peak (full width at half maximum, FWHM), K is the Scherrer constant and θ is the Bragg angle.   The weight ratio of rutile phase (W_R) can be estimated by the sub-equation

$$W_R = \frac{A_R}{0.884 A_A + A_R} \tag{3-4}$$

where A_A is intensity of anatase (101) peak and A_R is intensity of rutile (110) peak.

3-3-6 X-ray photoelectron spectroscopy (XPS)

The X-ray photoelectron spectroscopy (XPS, ESCA PHI 1600 spectrometer) was used to identify the surface chemical compositions and chemical state by using the AlKα radiation (1486.6 eV).   All the analytical process in the chamber was controlled under ultrahigh vacuum at the pressure below 1.4 ×10^{-9} Torr.   The collection step sizes in wide range scan

and high-resolution analysis are 1.0 eV and 0.1 eV, respectively.   The C 1s peak at 284.8 eV was used to be the reference.   The integrated peak areas of spectra were estimated using sensitivity factors to determine the surface atomic ratios.   The equation for atomic ratio is calculated by the sub-equation

$$\frac{n_1}{n_2} = \frac{I_1/ASF_1}{I_2/ASF_2} = \frac{A_1/ASF_1}{A_2/ASF_2} \qquad (3\text{-}5)$$

where n means the atomic numbers, I means the intensity of species on XPS spectra, A is the peak area, *ASF* stands for the atomic sensitive factor of element and Arabic number represents elemental types.

3-3-7 Electron paramagnetic resonance (EPR)

The electron paramagnetic resonance spectrometer (EPR, Bruker EMX-10/12) was used to examine the photo-induced charge carriers at X-band frequency.   The measurements were carried out at 77 K in darkness or under irradiation.   The conditions of the instrument were set at a center field of 3500 G and a sweep width of 2000 G.   The microwave frequency was 9.49 GHz and the power was 1.0 mW.

3-3-8 Gas chromatograph (GC)

The gaseous sample after photolysis was analysed using gas chromatography (GC, Thermo TRACE GC Ultra) using a FS Cap Supel-Q PLOT column of 30 m length with a diameter of 0.53 mm.   Helium was used as a carrier gas.   Thermal conductivity detector (TCD) and flame ionization detector (FID) were used for analyzing the gaseous samples, such as CH_4, CH_3OH.etc.

The calibration curve is used to determine the concentration of the CH_4 production. First, the pure N_2 gas purged the reactor for 1 hour to ensure the air was eliminated.   After closed the valves, 10 μL CH_4 was injected into the reactor.   Then, 20 μL, 50 μL, 100 μL, 200 μL, 300 μL, 400 μL and 500 μL of gas in reactor were detected by GC to establish the calibration curve.   Appendix D-1 shows the calibration curve of CH_4.

3-3-9 X-ray absorption (XAS)

The X-ray absorption (XAS) spectra was used to identify the valence of the vanadium ions within the TiO_2 lattice recorded at BL 16A at Taiwan Synchrotron Radiation Research Center (NSRRC).   The measurements were carried out at Ambient temperature.   The V K-edge spectrum was received using a fluorescence mode.   The linear absorption coefficient (μ) was estimated in term of the ratio between incident (I_0), fluorescence intensities (I_f). The following equation can be expressed by sub-equation:

$$\mu_{fluorescence}(E) \propto I_f/I_0 \tag{3-6}$$

3-4 Photocatalytic reduction of CO$_2$

First, the 0.05 g samples were loaded on the Glass fiber filter paper(ADVANTEC GC-50), then filter paper was placed in the middle of reactor.   The reactor has the size of 50 mm (length) × 74 mm (diameter) and the total volume of 220 ml.   The reactor was covered by a quartz glass that can let UV light passing through as shown in Figure 3-1.   Carbon dioxide (99.9%) is splitted into two pipelines, which one is for dry CO$_2$ and the other one flowed through the DI water for humidification.   The different split ratios of these two streams can be adjusted the humidity in the system, which was set about 90% in this study (as shown in Figure 3-2).   In our case, the catalysts were pretreated by heated (heating) at 120 °C for 1h in air and were irradiated with the UV light (λ<305nm) for 12 hours.   The magnet stirred to homogenize the gaseous system through the photocatalysis.   Prior to the photoreduced experiments, the humidified CO$_2$ gas purged the reactor for 1 hour to ensure the air was eliminated.   After that, the valves located at outlet and inlet of the reactor were closed.   Then, UV irradiation of the catalysts was carried out under irradiation of 16 UV lamps (8 W) at 305 nm for 8 hours.   Figure 3-3 displays the photograph of the photocatalytic system.

Quantum efficiency is generally used to universally evaluate the photocatalytic performance of a certain photocatalyst and system design.   The quantum efficiency therefore depends on both the collection of charges and the absorption of light.   Since eight moles of electrons are required to produce 1 mol of methane from CO$_2$, the quantum efficiency of a photocatalyst for photocatalytic conversion of CO$_2$ to CH$_4$ is expressed as Equation 3-7.

$$\text{quantum efficiency (\%)} = \frac{8 \times \text{moles of methane yield}}{\text{moles of incident UV photon}} \times 100 \qquad (3\text{-}7)$$

The equation for moles of UV photon absorbed by catalyst is calculated by the sub-equation.

$$\text{moles of incident UV photon} = \frac{\text{Absorbed photon flux (W/cm}^2) \times \text{SA (cm}^2) \times \text{T (s)}}{\text{Each photon energy (J)} \times 6.02 \times 10^{23}} \qquad (3\text{-}8)$$

In our study, the absorbed photon flux detected by photometer is 1.2×10^{-4} W/cm^2. The surface area received UV-light is 8.042 cm^2. T means the radiation time. The each photon energy at 305 nm wavelength is 6.517×10^{-19} J.

Figure 3-1 A photograph of the reactor for photocatalytic reduction.
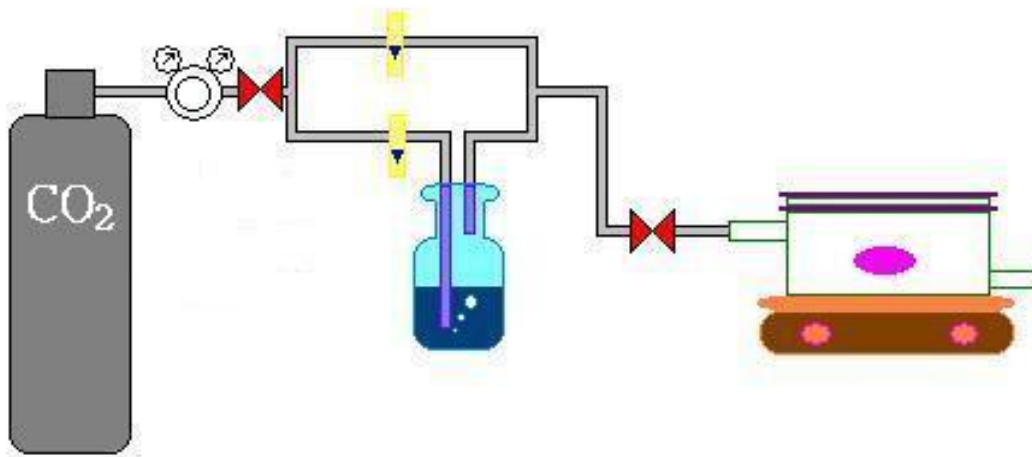
Figure 3-2 An apparatus design for photocatalytic reduction of CO_2.
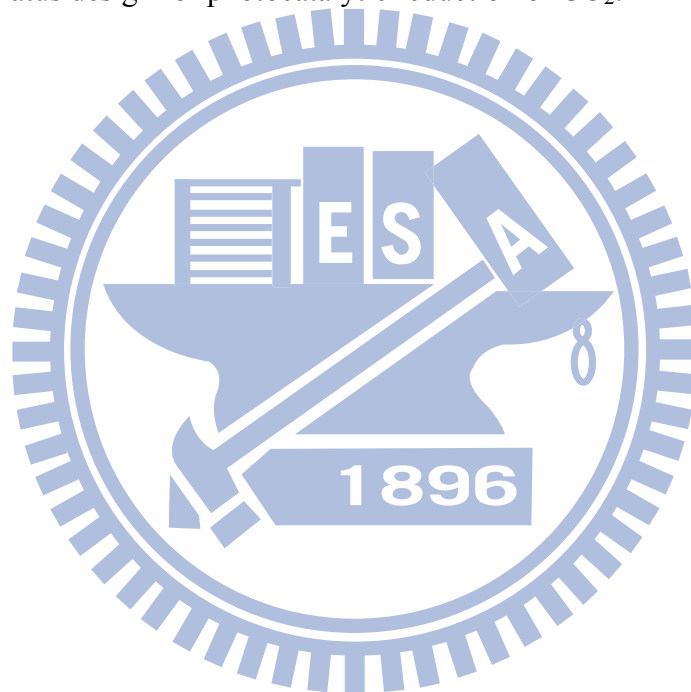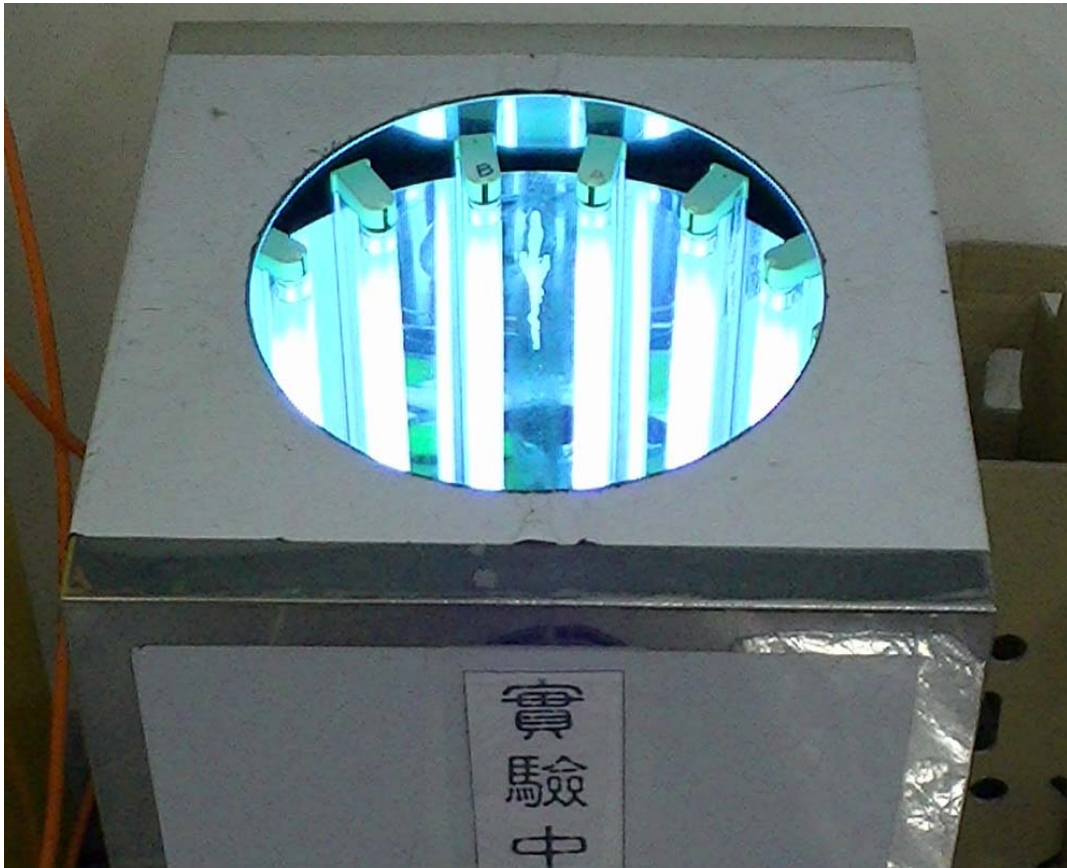
Figure 3-3 A photograph of the lamping system.

Chapter 4. Results and Discussion

4-1 Chemical compositions

To understand the chemical states and chemical compositions of the vanadium ions at the surface sites and in the bulk lattice of the doped TiO_2, the V-doped TiO_2 samples calcined at different temperatures were characterized using SIMS, ICP-MS, XPS, XAS, and EPR. Table 4-1 lists the bulk and surface V/Ti ratios of 1.00 and 0.01 at.% V-doped TiO_2. The total V/Ti ratios in the 1.00 at.% V-doped TiO_2 calcined at 200 and 500 °C were 1.03×10^{-2}, which were similar to the added one, indicating the non-volatility of the vanadium ions in the TiO_2 matrix. Although the surface V/Ti ratio at 200 °C (1.17×10^{-2}) was close to the total ratio (1.03×10^{-2}), the surface V/Ti ratio increases when the calcination temperature increased and reaches 7.6 times when the calcination temperature increased to 600 °C (8.86%). The total V/Ti ratios in the 0.01 at.% V-doped TiO_2 calcined at 200 and 500 °C were 1.15×10^{-4} and 1.04×10^{-4}, respectively, also indicating the non-volatility of the vanadium ions in the TiO_2 matrix. The surface V/Ti ratios in the 0.01 at.% V-doped TiO_2 increases 2.95 times when the calcination temperature increased from 200 (1.15×10^{-4}) to 600 °C (3.39×10^{-4}), which were similar to the 1.00 at.% V-doped TiO_2. This phenomenon reveals the diffusion of the vanadium ions from the inside lattice to the surface. Davidoson and Che[29] reported that metal ions migrate to the surface of matrix above the Tammann temperature at which the thermal vibrations of cations are strong enough for lattice diffusion. Since the Tammann temperature of V_2O_5 is 209 °C, some vanadium ions migrated from bulk lattice toward to surface lattice of TiO_2 above this temperature in this study.

Figure 4-1 shows the V 2p XP spectra of the 1.00 at.% and 4.00 at% V-doped TiO_2 calcined at different temperatures. The V 2p photoelectron lines of the 1.00 at.% V-doped TiO_2 were insignificant after calcination at 200 °C. Whereas, the sample showed the V $2p_{3/2}$

and $2p_{1/2}$ peaks centered at 517.5 and 524.3 eV, respectively, at 700 °C.[54] Similar result

was found in the 4.00 at.% V-doped TiO_2 sample at 200 °C. These phenomena reveal that

V^{5+} ions were mainly at the TiO_2 surface, and again prove that their concentration increased

with calcination temperature. Figure 4-2 shows the V K-edge XA spectra of the 1.00 at.%

V-doped TiO_2. The XAS shows the pre-edge absorptions of the V^{3+}, V^{4+} and V^{5+} ions at

5469.9, 5470.3 and 5470.6 eV, respectively, indicating the reduced V ions within the TiO_2

lattice.[35, 55-57] The intensity variation is noteworthy. The intensity increases with

increasing calcination temperature. The result shows the square-pyramidal symmetry (as in

V_2O_5) gradually formatted when increasing calcination temperature.[58] The rising-edge

energy values shift from 5481.5 to 5482 eV. The result indicates the valence state of

vanadium transformed to higher state.[56, 59-61] The V^{3+} and V^{4+} ions contributed a large

portion at low temperatures, and they were gradually transformed to the V^{5+} state at elevated

temperatures. Since the transformation occurred along with the thermal induced migration

of the V ions, the oxidation of V^{3+}/V^{4+} was possibly resulted from their interaction with O_2 in

the atmosphere when the reduced ions diffused to the surface. The XAS shows the

near-edge appeared two peaks at 5492 and 5550 eV when calcination temperature above 600

°C. According to the literature, at temperature above to 600 °C, the V^{4+} ions are

incorporated within the rutile structure.[62]

Figure 4-3 shows the EPR spectra of the 1.00 at.% V-doped TiO_2 at different calcinations

temperatures in the dark at 77K. In this study, the hyperfine structure of V^{4+} ions were

resulted from the interaction between the vanadium nucleus spin (I=7/2) and the unpaired $3d^1$

electron. The peaks at 300 and 400 °C show the following EPR parameters: $g_\perp$ =1.959, $A_\perp$

=57 G and $g_{//}$ =1.917 , $A_{//}$ =173 G. [63-65] This results indicate that there are V^{4+} ions in

the anatase phase of the V-loaded sample. When the calcination temperature increases from

300 to 600 °C, the intensity of the peaks are decreased. The results indicate that the phase

transformed to the rutile phase. However, the peaks at 500 and 600 °C show another

following EPR parameters: $g_{xx}, g_{yy} = 1.913$, $A_{xx} = 31$ G, $A_{yy} = 43$ G and $g_{zz} = 1.956$, $A_{zz} = 152$ G.[63, 66] This results indicate that there are V^{4+} ions in the rutile phase of the V-loaded sample. Because the XPS spectrum indicates the vanadium on the surface are V^{5+} ions, V^{4+} ions are indicated in the bulk of TiO_2.[62] Figure 4-4 shows the EPR spectra of the 0.01 at.% V-doped TiO_2 at different calcinations temperatures before and after UV irradiation at 77K. The peaks at 300 and 400 °C show the following EPR parameters: $g_{\perp} = 1.986$.[67] This results indicate that there are V^{4+} ions in the interstitial sites in the anatase phase of the V-loaded sample. This signals decrease when the calcination temperature increased from 300 to 600 °C. The results indicate that the phase transformed to the rutile phase. However, The peaks at 500 and 600 °C indicate another following EPR parameters: $g_{xx}, g_{yy} = 1.913$, $A_{xx} = 31$ G, $A_{yy} = 43$ G and $g_{zz} = 1.956$, $A_{zz} = 152$ G. This results show that there are V^{4+} ions in the rutile phase of the V-loaded sample. Table 4-2 lists the g=factor of EPR.
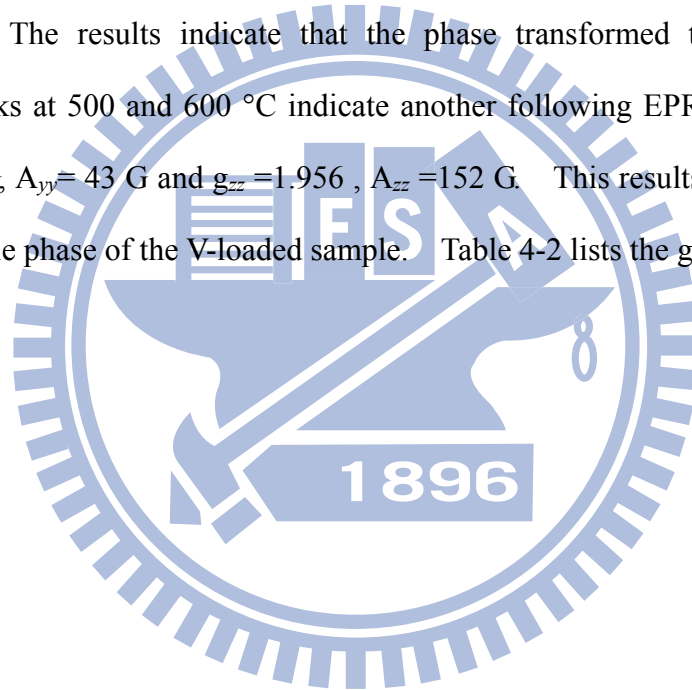
Table 4-1 The bulk and surface V/Ti atomic ratios of doped TiO_2.

Added V/Ti ratios	calcination temperature	Bulk V/Ti ratios (ICP-MS)	Surface V/Ti ratios (SIMS)
1.00 at.% V/Ti	200 °C	1.03×10^{-2}	1.17×10^{-2}
1.00 at.% V/Ti	300 °C	1.08×10^{-2}	2.08×10^{-2}
1.00 at.% V/Ti	400 °C	1.07×10^{-2}	4.48×10^{-2}
1.00 at.% V/Ti	500 °C	1.03×10^{-2}	8.51×10^{-2}
1.00 at.% V/Ti	600 °C	1.14×10^{-2}	8.86×10^{-2}
0.01 at.% V/Ti	200 °C	1.15×10^{-4}	1.15×10^{-4}
0.01 at.% V/Ti	300 °C	0.94×10^{-4}	1.21×10^{-4}
0.01 at.% V/Ti	400 °C	1.38×10^{-4}	1.89×10^{-4}
0.01 at.% V/Ti	500 °C	1.04×10^{-4}	2.56×10^{-4}
0.01 at.% V/Ti	600 °C	1.26×10^{-4}	3.39×10^{-4}
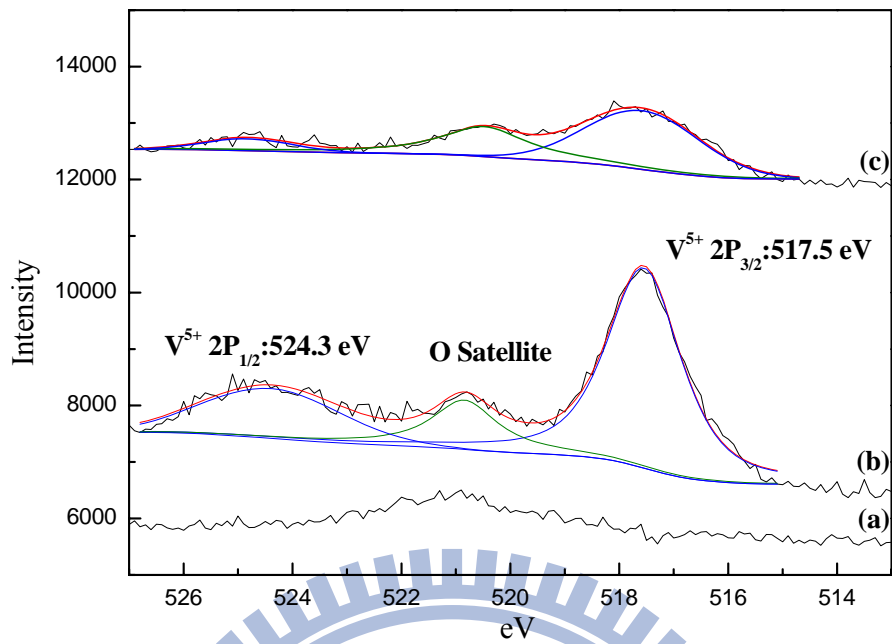
Figure 4-1 The XPS spectra of (a) 1.00 at.% V-doped TiO$_2$ at 200 °C, (b) 1.00 at.% V-doped

TiO$_2$ at 700 °C and (c) 4.00 at.% V-doped TiO$_2$ at 200 °C.
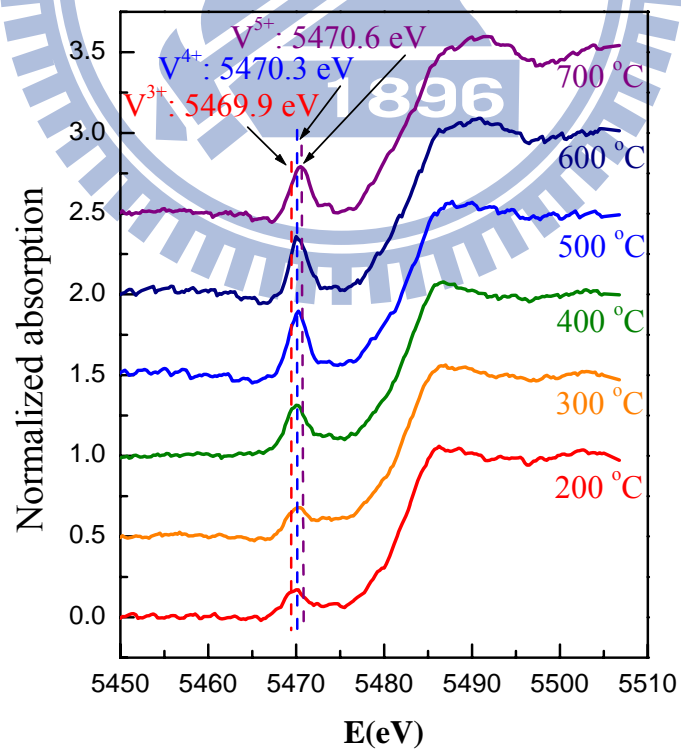
Figure 4-2 The V K-edge XA spectra of the 1.00 at.% V-doped TiO$_2$.
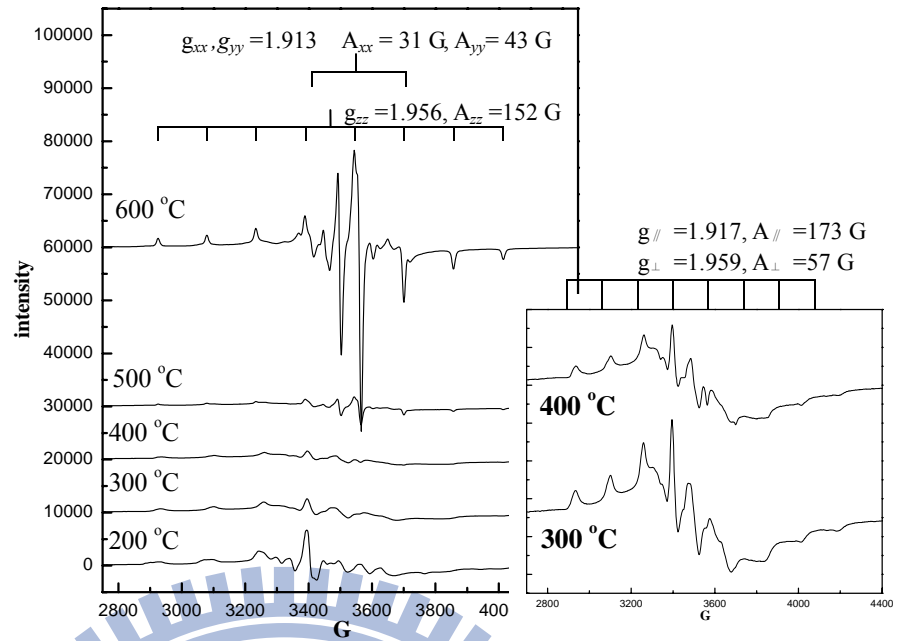
Figure 4-3 EPR spectra of 1.00 at.% V-doped TiO_2 at different calcination temperature at 77K in the dark.
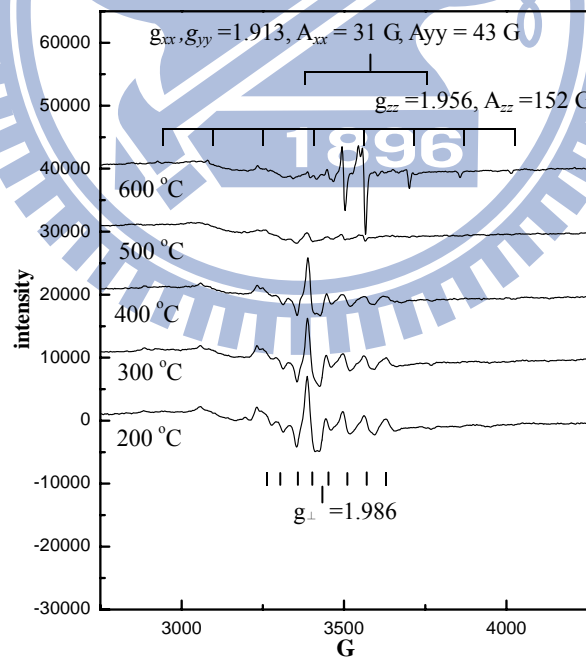
Figure 4-4 EPR spectra of 0.01 at.% V-doped TiO_2 at different calcination temperature at 77K in the dark.

Table 4-2 EPR Parameters of Paramametic Swcies in the pure TiO_2 and V-doped TiO_2.

g factor	assignment	Ref.
EPR Parameters of Ti^{3+} (electron center) Radicals		
$g_1=1.990$; $g_2=1.990$; $g_3=1.960$	Ti^{3+} (hydrated anatase)	[68]
$g_1=1.961$; $g_2=1.992$; $g_3=1.992$	Ti^{3+} (colloidal TiO_2)	[69]
$g_\perp=1.990$; $g_{//}=1.957$	Ti^{3+} (anatase)	[70]
$g_\perp=1.975$; $g_{//}=1.940$	Ti^{3+} (rutile)	[70]
$g_\perp=1.925$; $g_{//}=1.885$	Ti^{3+} (surface Ti^{3+} in colloidal TiO_2)	[71]
EPR Parameters of Oxygen Related Signals (hole center)		
$g_1=2.004$; $g_2=2.009$; $g_3=2.023$ $g_\perp=2.022$; $g_{//}=2.004$ $g_1=2.003$; $g_2=2.008$; $g_3=2.035$	organic peroxyl (e.g., $ROO^{\cdot}$) carboxyl radical of cysteine $(CH_3)_3N^+CH_2OO^{\cdot}$	[72]
$g_1=2.003$; $g_2=2.009$; $g_3=2.024$ $g_1=2.003$; $g_2=2.009$; $g_3=2.025$ $g_1=2.003$; $g_2=2.009$; $g_3=2.021$	Ti^{4+}-O_2^- on anatase	[68, 69, 72]
$g_1=2.002$; $g_2=2.009$; $g_3=2.034$ $g_1=2.002$; $g_2=2.003$; $g_3=2.034$	Ti^{4+}-O_2H	[72]
$g_1=2.002$; $g_2=2.016$; $g_3=2.028$ $g_1=2.004$; $g_2=2.018$; $g_3=2.030$ $g_1=2.007$; $g_2=2.019$; $g_3=2.027$	Ti^{4+}-O^{2-}-Ti^{4+}-O^- (O_s^-)	[69, 72]
$g_1=2.002$; $g_2=2.007$; $g_3=2.011$ $g_1=2.003$; $g_2=2.009$; $g_3=2.014$ $g_1=2.003$; $g_2=2.003$; $g_3=2.009$	Ti^{4+}-O_3^-	[72]
$g_1=2.003$; $g_2=2.013$; $g_3=2.024$ $g_1=2.007$; $g_2=2.014$; $g_3=2.024$ $g_1=2.002$; $g_2=2.012$; $g_3=2.016$ $g_1=2.004$; $g_2=2.014$; $g_3=2.018$	Ti^{4+}-O^--Ti^{4+}-OH^- (O_B^-)	[72]
$g_1=2.001$; $g_2=2.009$; $g_3=2.021$	$O_2^{-\cdot}$ (on anatase)	[73]

EPR Parameters of V4+ sites in TiO$_2$		
$g_\perp$=1.981; $g_{/\!/}$=1.924	V^{4+} (in anatase)	[63, 67]
g_1=1.906; g_2=1.960; g_3=1.960		
g_1=1.917; g_2=1.959; g_3=1.959		
g_1=1.913; g_2=1.913; g_3=1.956	V^{4+} (in Rutile)	[63, 66]
g_1=1.912; g_2=1.914; g_3=1.956		
g_1=1.923; g_2=1.986; g_3=1.965	V^{4+} (in Interstitial Sites in Anatase)	[63]
g_1=1.923; g_2=1.967; g_3=1.940		

4-2 Microstructures

To examine the effect of the thermal-induced migration on the crystalline phase, grain size, specific surface area and bandgap, the samples were analyzed by using XRD and BET. Figure 4-5 to Figure 4-7 shows the XRD patterns of the pure, 1.00 at.% and 0.01 at.% V-doped TiO_2 at different calcination temperatures, respectively. The anatase and rutile phase were indentified from the their typical (101) and (110) diffraction peaks at 25.4 and 27.5° 2θ positions, respectively. Table 4-3 lists the crystalline structures, surface areas and bandgaps of the pure and V-doped TiO_2 after the calcination at different temperatures. The pure TiO_2 contained anatase phase above 200 °C. The phase transformation from anatase to rutile took place at 600 °C. However, the incorporation of V ions into the TiO_2 lattice accelerated the phase transformation and resulted in a lower phase transit temperature of 500 °C. The decreased stability of anatase phase was presumably due to the formation of V_2O_5 on the surface. The differential weight loss curves (shown in Figure 4-8) of the V-doped TiO_2 show two peaks at 606 and 830 °C for 1.00 at.% and 0.01 at.% V-doped TiO_2, respectively, indicating the formation of V_2O_5 moiety.[74-76] We further used GIXRD to analyze the surface structures of the doped TiO_2 and the results were shown in Figure 4-9 and Figure 4-10. The 1.00 at.% V-doped TiO_2 contained a weak V_2O_5 diffraction at 19.12° 2θ position at 300 °C. This V_2O_5 diffraction peak became intensive at 600 °C, which is in agreement with the observation in the thermogravimetric analysis data. Amores and Balikdjian provided a model of "sintering-induced phase transition" to describe the thermal behavior that V ions lowered phase transit temperature.[77-79] In their model, surface V species causes inefficient heat dispersion during sintering and promotes nucleation of rutile phase at the surface boundaries. Thermal induced coalescence causes the surface areas of the pure TiO_2 decreasing from 131 to 1 m^2/g as the temperature increased form 200 to 600 °C. The V-doped TiO_2 exhibited similar surface areas (1-124 m^2/g for 0.01 at.% V-doped TiO_2;

2-135 m^2/g for 1.00 at.% V-doped TiO$_2$) at the same temperature range. Incorporation of V ions only slightly inhibited the sintering effect because of their low concentrations. The 0.01 at.% V-doped TiO$_2$ didn't exist any V$_2$O$_5$ diffraction at 19.12° 2θ position. Low concentrations of V ions don't have enough capacity to lead to the formation V$_2$O$_5$ moiety does not have enough capacity from 200 to 600 °C.

Figure 4-11 schematically illustrates the microstructures of the V-doped TiO$_2$ transformed from low to high calcination temperature. At lower temperatures, V^{3+}/V^{4+} ions disperses homogenously and interstitially within the TiO$_2$ lattice, while the V^{5+} ions mainly stay at the surface. Thermal treatment induces the migration of V^{3+}/V^{4+} ions moving from the inside TiO$_2$ matrix to its surface lattice and transforming to V^{5+} ions. As the concentration of the accumulated V^{5+} ions over its solubility in the TiO$_2$ matrix, they segregate from the TiO$_2$ matrix to form V$_2$O$_5$ moiety.
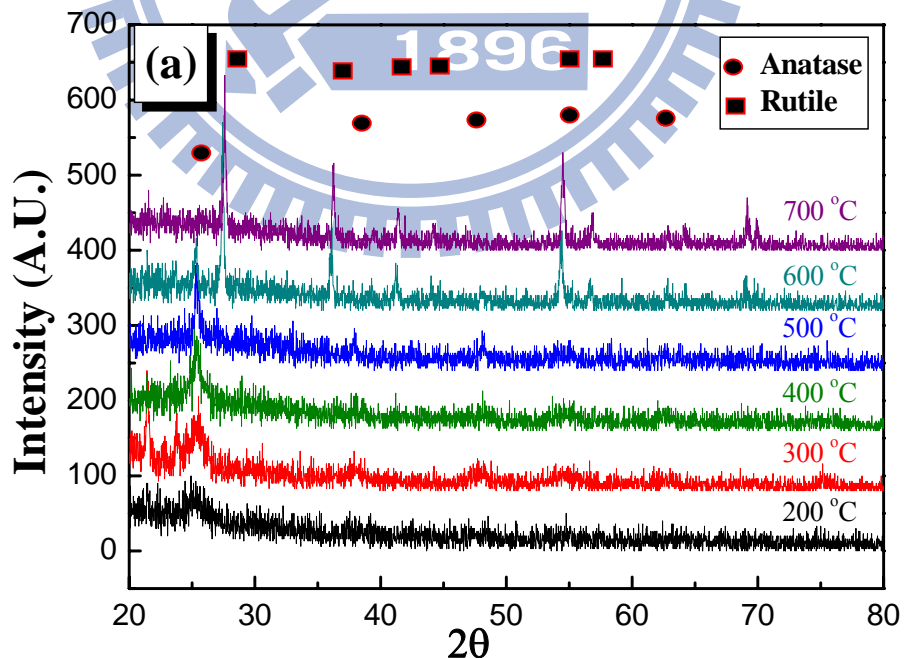
Figure 4-5 The XRD patterns of the pure TiO$_2$ at different calcination temperatures.
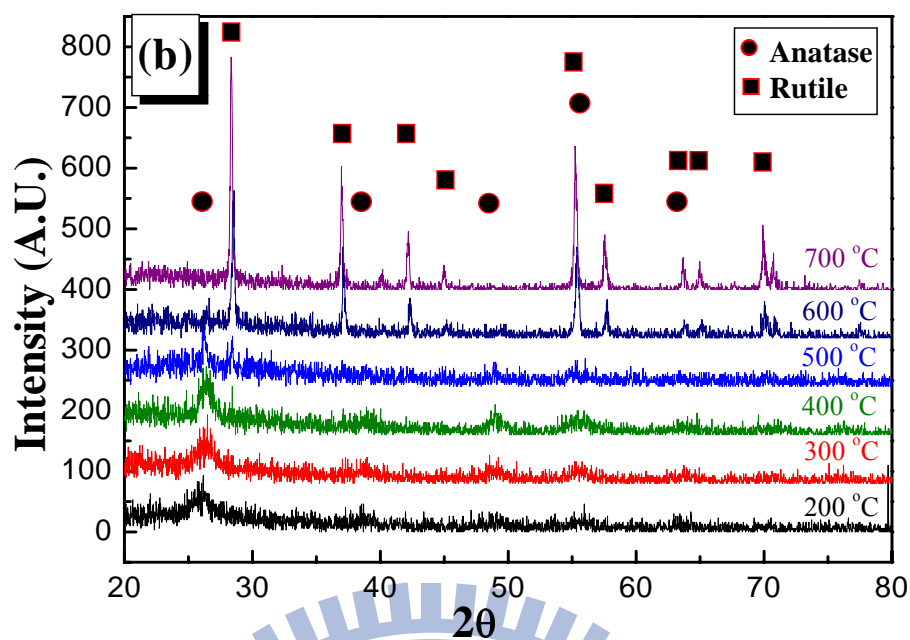
Figure 4-6 The XRD patterns of the 0.01 at.% V-doped TiO_2 at different calcination temperatures.
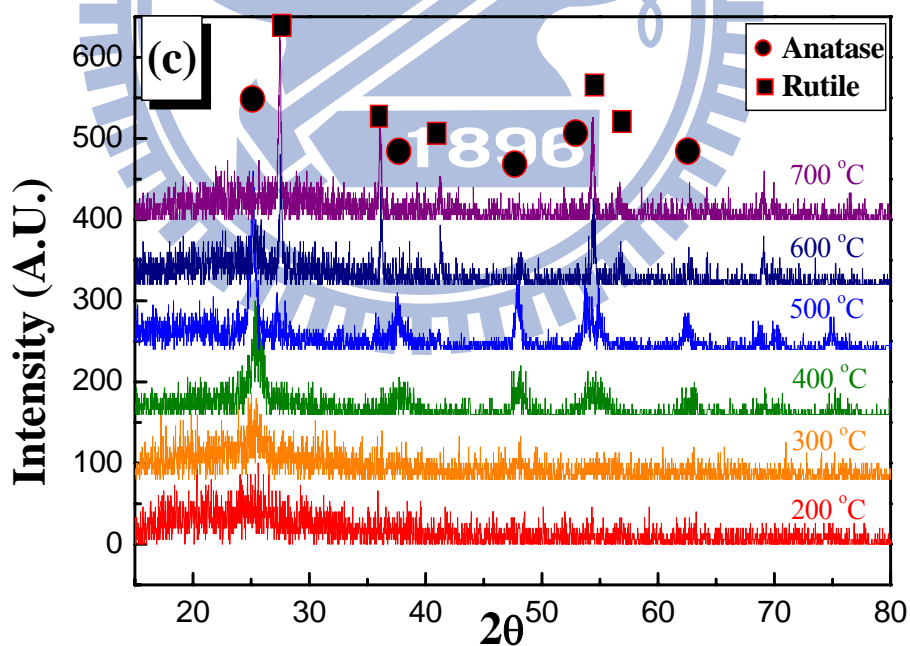
Figure 4-7 The XRD patterns of the 1.00 at.% V-doped TiO_2 at different calcination temperatures.

Table 4-3 The crystalline properties, surface areas and bandgaps of the pure TiO_2 and V-doped TiO_2 calcined at different temperatures.

Samples	calcination temperature	Crystal phase	D^a (nm)	SA^b (m^2/g)	Band gap
pure TiO_2	200 °C	A	2.4	131	3.3 eV
	300 °C	A	4.6	104	3.3 eV
	400 °C	A	8.1	68	3.2 eV
	500 °C	A	23.0	10	3.1 eV
	600 °C	A/R (26/74)	26.4/30.0	2	3.0 eV
	700 °C	R	35.4	1	3.0 eV
0.01 at.% V-doped TiO_2	200 °C	A^d	4.7	124	3.2 eV
	300 °C	A	4.4	111	3.2 eV
	400 °C	A	7.4	78	3.1 eV
	500 °C	A/R^e (56/44)	26.9/30.1	14	3.0 eV
	600 °C	A/R (13/87)	49.2/37.8	2	3.0 eV
	700 °C	R	45.8	1	3.0 eV
1.00 at.% V-doped TiO_2	200 °C	A	2.6	135	1.6 eV
	300 °C	A	3.8	112	1.6 eV
	400 °C	A	6.8	75	1.6 eV
	500 °C	A/R (84/16)	19.5/24.7	12	1.6 eV
	600 °C	A/R (32/68)	26.4/28.9	8	1.6 eV
	700 °C	R	42.9	2	1.6 eV

[a] crystallite sizes, [b] surface area, [c] bandgaps, [d] anatase phase and [e] rutile phase.
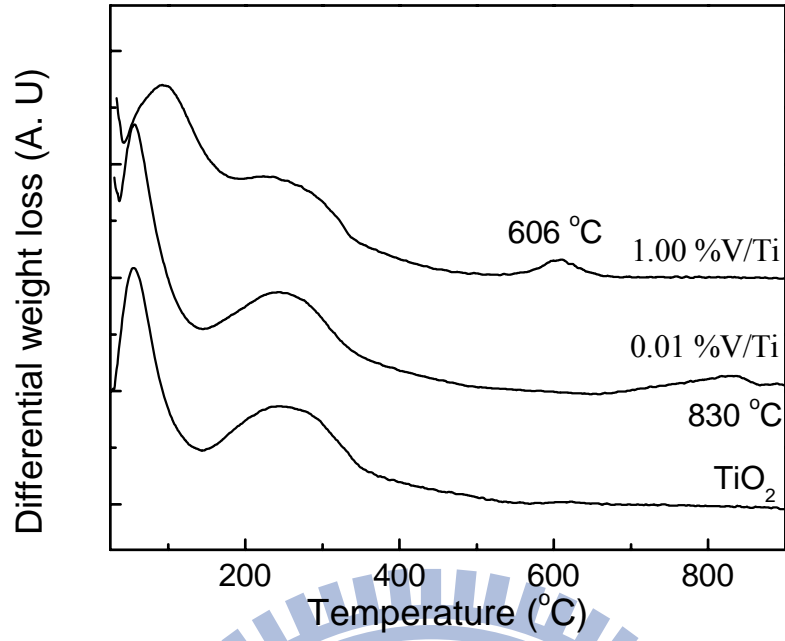
Figure 4-8 The differential weight loss curves of the pure, the 0.01 at.% and 1.00 at.% V-doped TiO_2.
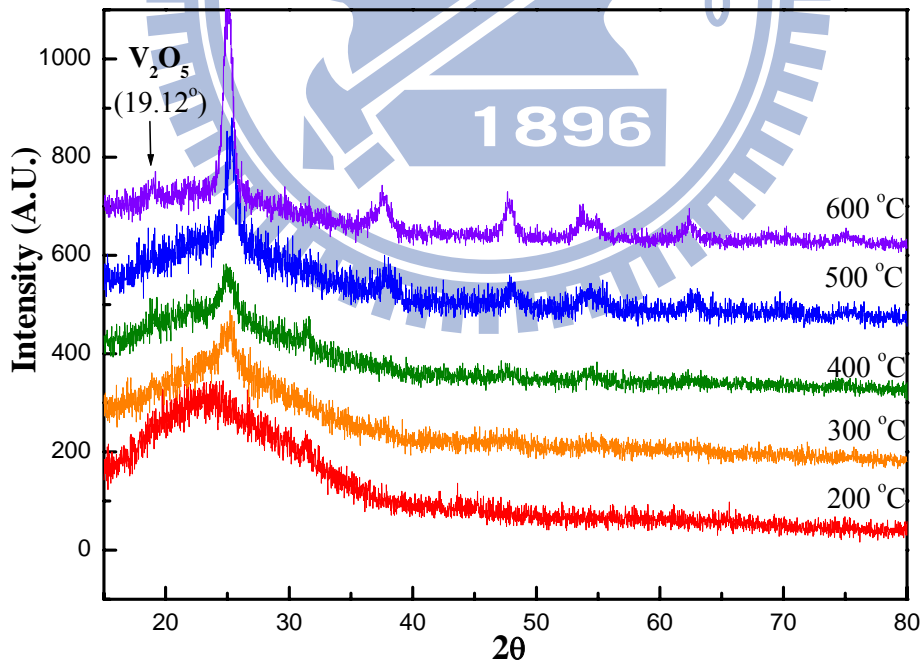
Figure 4-9 The GI-XRD patterns of the 1.00 at.% V-doped TiO_2 at different calcination temperatures.
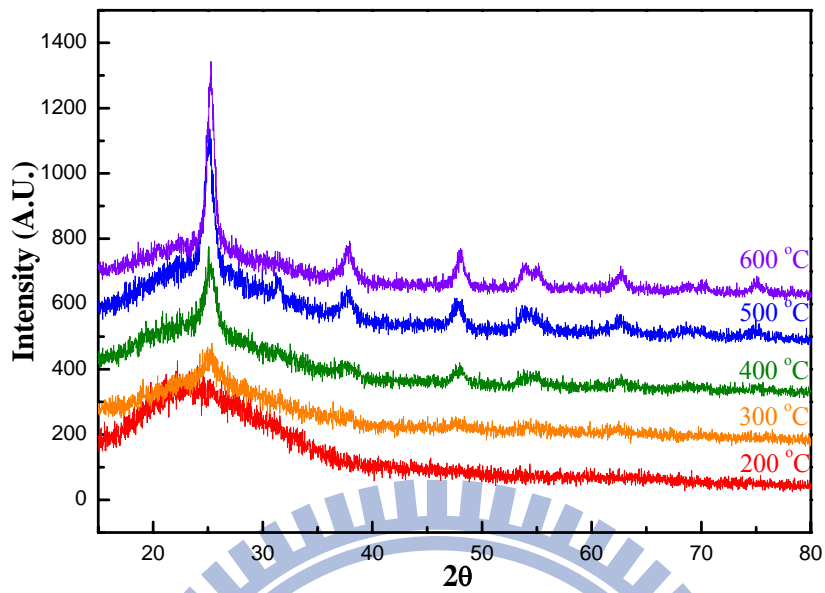
Figure 4-10 The GI-XRD patterns of the 0.01 at.% V-doped TiO_2 at different calcination temperatures.

V^{3+} and V^{4+} ions which were dispersed in the TiO_2 lattice

V_2O_5

Calcination temperature
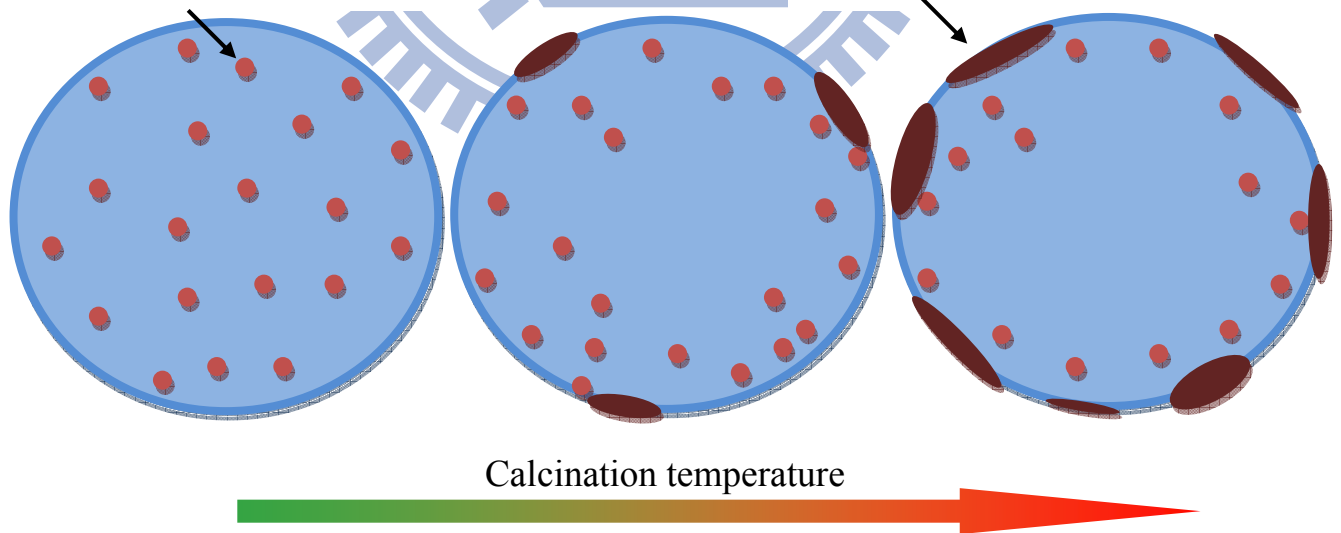
Figure 4-11 The microstructures of the V-doped TiO_2 transformed from low to high calcination temperatures.

4-3 UV-Visible absorption

To examine the electronic structures of the photocatalysts, the optical properties of the pure and V-doped TiO_2 samples were characterized in terms of UV-vis diffuse reflectance spectroscopy (DRS).   Figure 4-12 displays the optical absorbance of the pure TiO_2 and the 0.01 at.% V-doped TiO_2 at different calcination temperatures from wavelength of 900 to 200 nm. The bandgap energy of TiO_2 ranged 3.1-3.3 eV (absorption edge at 376-400 nm) below 600 °C, corresponding to the anatase.[17]   There were two bands below 405 nm. One broad band was ranged between 300-350 nm and centered at 340 nm which was denoted to lower CB.[80, 81] The other band centered at 233 nm was indicated to upper CB. When the calcination temperature was higher than 600 °C, the bandgap energy of TiO_2 shifted to 3.0 eV (413 nm) and lower CB center was ranged between 300-420 nm shifted to 362 nm because of generation of rutile phase decreased the bandgap range.[82]   The result can be ascribed to the formation of larger particles size therefore it decrease the quantum size effect.[82, 83] The spectra of the 0.01 at.% V-doped TiO_2 shows similar absorption behavior relative to the pure TiO_2.   The effect of the V ions with trance amounts on the electronic structure of TiO_2 sample was little to be detected.   Figure 4-13 displays the optical absorbance of the 1.00 at.% V-doped TiO_2 at different calcination temperatures.   The bandgap energy of the 1.00 at.% V-doped TiO_2 extended to 1.6 eV (779 nm). Chang *et al.*[35] reported that the occupied states of the V^{3+} and V^{4+} ions are located at 0.43 eV and 1.0 eV, respectively, below the bottom of the conduction band.   Thus, the long wavelength absorption could be resulted from the conduction band $\rightarrow$ semi-occupied V^{4+} state transition or the band-tail transition. This phenomenon of narrow bandgap to band-tail transitions result from the presence of amorphous structures in the V-doped TiO_2 grain-boundaries.[35]   Although some V_2O_5 crystals were distributed at the TiO_2 surface, their contents were too small to be detected by UV-vis spectrum.   Chang *et al.*[35] showed that the occupied states of the V^{3+} and V^{4+} ions

are located at 0.43 eV and 1.0 eV, respectively, below the bottom of the conduction band. The wavelengths for the V^{3+}/V^{4+} to conduction band are 1240 to 3100 nm. Therefore, the wavelengths were too long to be measured in this study. Figure 4-14 illustrates the possible electronic structure for the 1.00 at.%V-doped TiO_2. Chang at al.[35] indicated that the V^{3+} and V^{4+} ions in the TiO_2 crystals lead to electron-hole recombination.
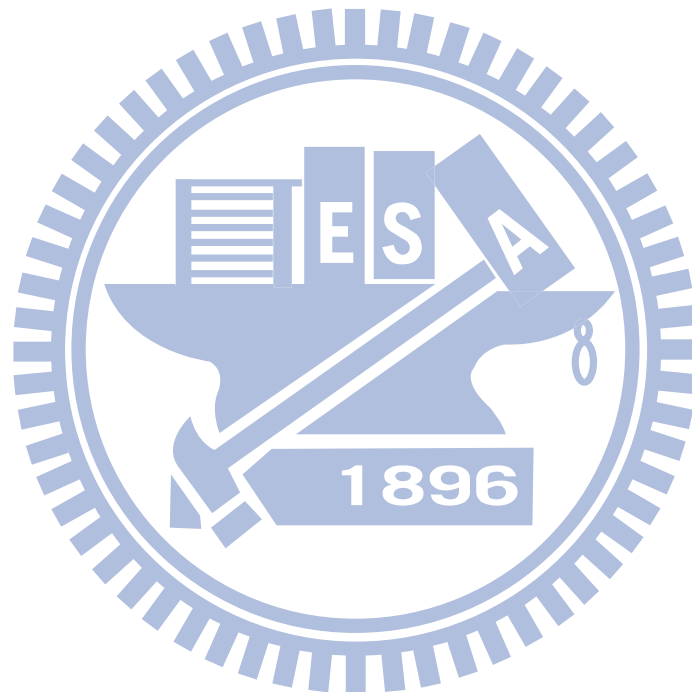
(a)
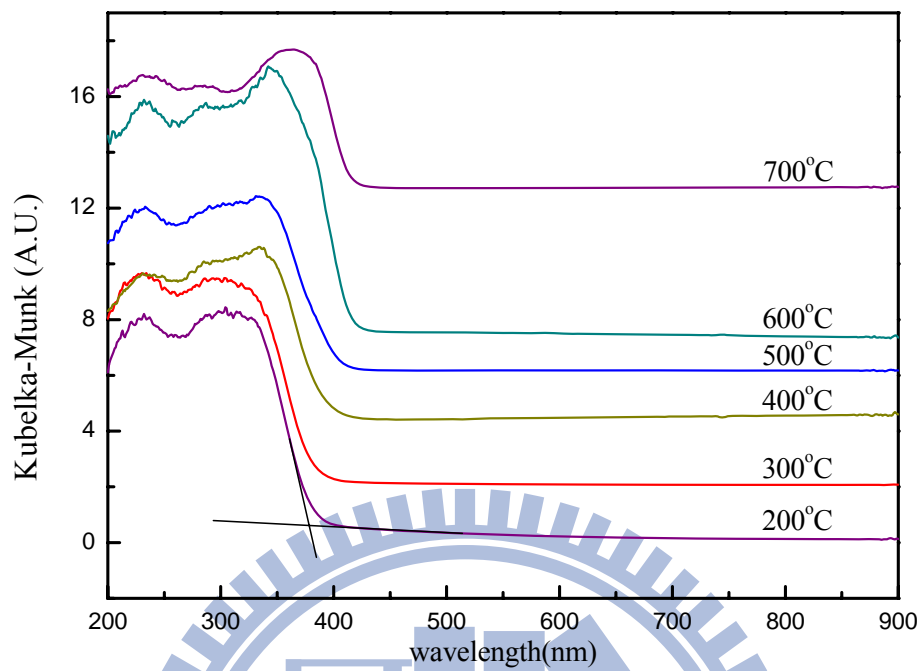
(b)

Figure 4-12 UV-Vis DRS spectra of (a)the pure TiO_2 and (b) the 0.01 at.% V-doped TiO_2 at different calcination temperatures.
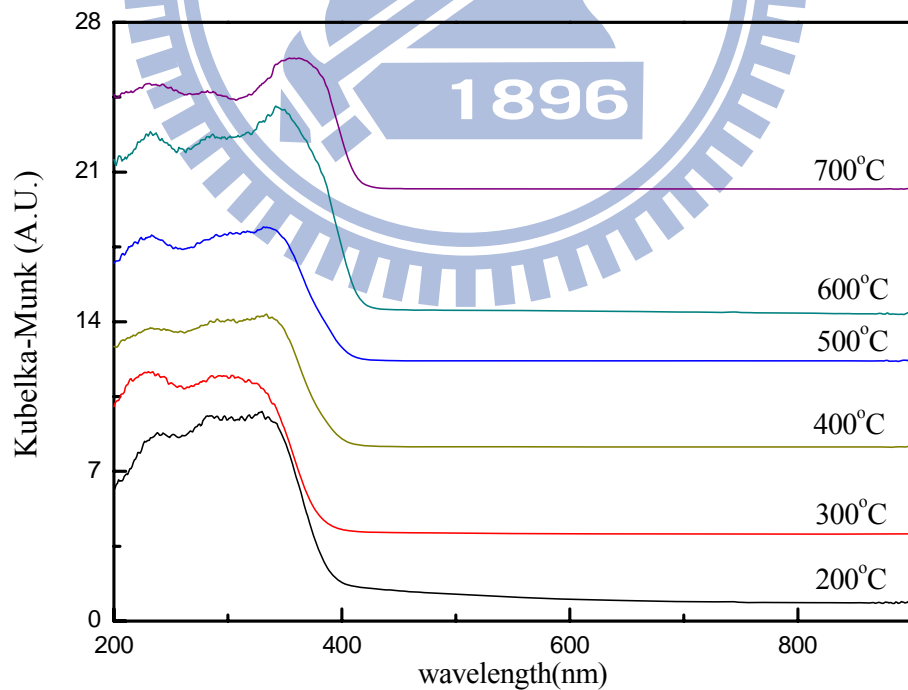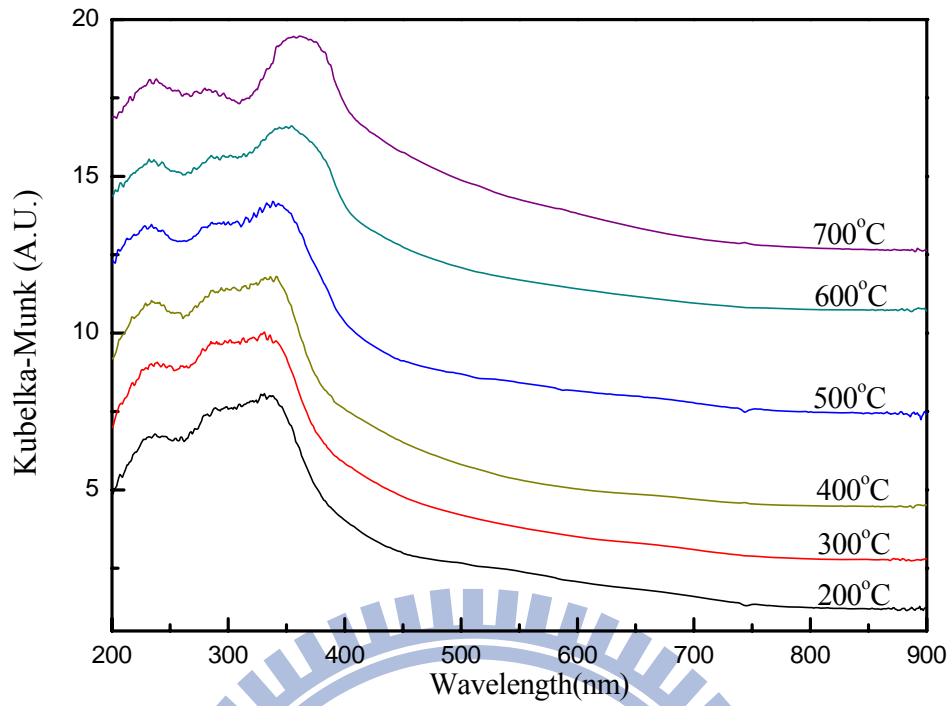
Figure 4-13 UV-Vis DRS spectra of the 1.00 at.% V-doped TiO_2.
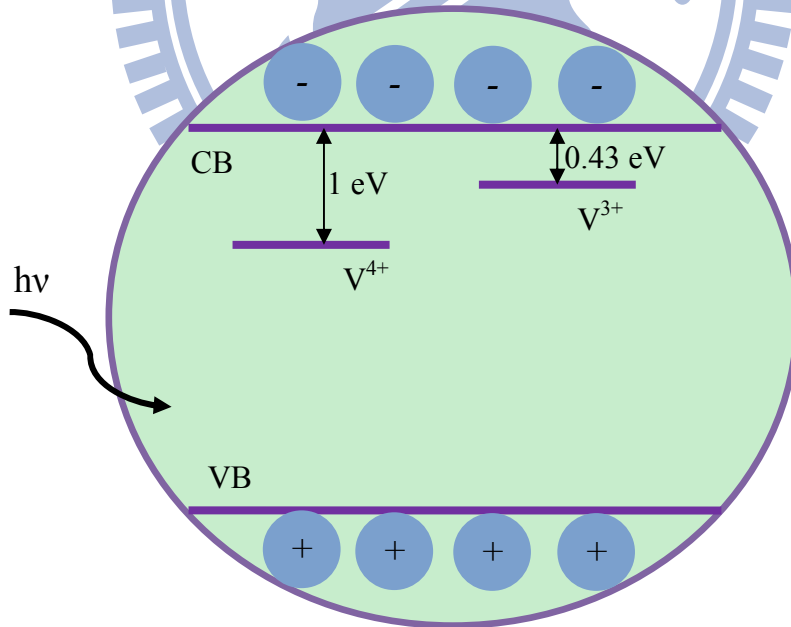
Figure 4-14 The electronic structure of 1.00 at.% V-doped TiO_2.

4-4 Photocatalytic activity

The photocatalytic activities of the pure TiO_2 and V-doped TiO_2 were examined in terms of the degradation of 0.01 mM RhB.   Figure 4-15 shows the rate constants of the pure and the V-doped TiO_2 samples calcined at different temperatures.   At 300-600 °C, the activity of the TiO_2 samples increased from 0.0216 to 0.445 with increasing temperatures.   Similar trend in the activities was found in the V-doped TiO_2-based systems till 500 °C.   The 0.01 at.% and 1.00 at.% V-doped TiO_2 showed their highest photocatalytic activities of 0.24 and 0.019 1/min, respectively, at 500 °C.   The activities of both the doped TiO_2 turned down at 600 °C.   The temperature dependent activity was mainly governed by crystallinity and phase compositions.   Smaller amounts of defects resulted at higher crystallinity led TiO_2 performing better photocatalytic efficiency. In addition, anatase and rutile composites promoted the activity because of well charge separations.[17, 20]   At 300-500 °C, 0.01 at.% V-doped TiO_2 exhibited higher activity than the pure TiO_2, indicating that trace amounts of V^{3+}/V^{4+} ions within the lattice preserve larger numbers of effective charge carriers for photocatalysis.   In contrast, the 1.00 at.% V-doped TiO_2 performed the lowest activity.   The lattice V^{3+}/V^{4+} ions either trap electrons or holes.   The trapped charge carries can not escape from the trapping sites and eventually annihilate inside the TiO_2 matrix.   Trace amounts of the impurities consume few charge carries from the bands to allow the remaining carriers successfully diffusing to the surface for interfacial transfer.   However, over amounts of defects lead to severe electron-hole recombination, thus remarkably inhibiting the photocatalytic efficiency.[35]

For examining the photoreduction activities of the V-doped TiO_2 the samples calcined at 400-600 °C were selected because their efficiencies for the photo-oxidation of RhB were higher than the samples calcined at the other temperatures.   All these reactions were carried out under the same irradiation condition as that for photocatalytic oxidation of RhB. CH_4

was the only product which was detectable in this study. Figure 4-16 shows the accumulated amounts of CH_4 in the presence of the pure and the 0.01 V-doped TiO_2. The pure TiO_2 calcined at 500 and 600 °C exhibited similar trend in the CH_4 generation. The yield of CH_4 rose fast in the first hour and reached almost a steady state till the eight hour. Calcination at 500 °C resulted the pure TiO_2 in a higher reductive activity than calcination at 600 °C. The CH_4 yield of the TiO_2 at 500 and 600 °C at the first hour was 0.66 and 0.54 µmol/g, respectively. The TiO_2 calcined at 400 °C performed a relatively low CH_4 yield (0.39 µmol/g) at the first hour. However, its CH_4 yield continuously increased to 0.66 µmol/g after 2 hours. After that, the yield decreased with the irradiation time and reached 0.58 µmol/g after 8 hr irradiation. Because substantial CO_2 and H_2O vapor still existed in the photoreductive system, the inhibited generation of CH_4 reveals its fast re-oxidation. Compared to the TiO_2 calcined at 400 °C, the sample calcined at higher temperatures (500-600 °C) showed higher initial activities for CO_2 reduction and retarded re-oxidation.

The photoreductive behavior of the 0.01 at.% V-doped TiO_2 samples calcained at 500 °C was similar to that of the pure TiO_2 at the same temperature. It produced 0.54 µmol/g of CH_4 yield in the first hour and kept a steady accumulated yield in the last 7 hours. The sample calcined at 600 °C resulted in 0.35 µmol/g of CH_4 yield in the first hours. The accumulated yield constantly increased with the irradiation time and reached 0.52 µmol/g at the eighth hour. Calcination at 400 °C exhibited the highest accumulated yield (0.57 µmol/g) at the third hour. Afterwards, the yield was maintained till the eight hour.

The yield of CH_4 in the pure TiO_2 and 0.01 at.% V-doped TiO_2 systems either kept similar or decreased after the maximum has reached. However, the 1.00 at.% V-doped TiO_2 samples show different phenomenon. The samples calcined at 400-600 °C all continuously increased the CH_4 yield with the irradiation time (Figure 4-17). The yields of CH_4 reached 0.77, 1.17 and 0.94 µmol/g in the presence of the samples calcined at 400, 500 and 600 °C, respectively.

49

Quantum efficiency, which is the ratio between the moles of products and moles of photons incident, is generally used to universally evaluate the photocatalytic performance of a certain photocatalyst and system design.   Since eight moles of electrons are required to produce 1 mol of methane from CO_2, the quantum efficiency of a photocatalyst for photocatalytic conversion of CO_2 to CH_4 is expressed as Equation 4-1.

$$\text{quantum efficiency (\%)} = \frac{8 \times \text{moles of methane yield}}{\text{moles of UV photon absorbed by catalyst}} \times 100 \qquad (4\text{-}1)$$

The QE in the first hour is taken to compare the initial activities of the photocatalysts, while the QE after 8-hr irradiation was referenced to understand the reductive behavior.   Table 4-4 lists the quantum efficiency of the pure TiO_2 and V-doped TiO_2.   Figure 4-18 shows the quantum efficiency of the pure TiO_2, 1.00 and 0.01 at.% V-doped TiO_2 after 1-hr and 8-hr irradiation.   The pure TiO_2 photocatalyst calcined at 500 °C exhibited the highest QE of 2.98 % over the photocatalysts prepared under different conditions in this study. Table 4-5 lists some references of photoreduction of CO_2.   Li et al.[84] synthesized mesoporous silica supported Cu/TiO_2 nanocomposites and carried out photoreduction experiments in a continuous-flow reactor using water vapor and CO_2 under UV-light irradiation.   The high surface area mesoporous silica substrate enhanced CO_2 photoreduction and the QE of CH_4 reached 0.28%.   Wu et al.[6] designed catalyst-coated fibers to transmit and spread light inside the reactor under UV irradiation.   The rate of the yield of methanol was 4.12 µmole/g-cat h and the QE reached 0.00013%.   Varghese et al.[85] used N-doped titania nanotube arrays to converse CO_2 and water vapor to hydrocarbons by outdoor global AM 1.5 sunlight.   This hydrocarbon production rate was 111 ppm cm^{-2} h^{-1} and QE reached 0.74%. The highest QE in this study is significantly high compared to the references.   Incorporated V ions into the TiO_2 lattice either at 0.01 at.% or 1.00 at.% inhibited the activities.   The 0.01 at.% V-doped TiO_2 inhibited the initial activities of the pure TiO_2 samples calcined at 400,

500 and 600 °C by 0.97, 0.82 and 0.65 fold, respectively, while the 1.00 at.% V-doped TiO_2 inhibited the activities by 0.92, 0.89 and 0.74 fold, respectively.   However, the quantum efficiency in V-doped TiO_2 showed higher QEs after irradiation of 8 hours.   Relative to the pure TiO_2 calcined at 400, 500 and 600 °C, the 1.00 at.% V-doped TiO_2 improved the QE of CH_4 by 1.33, 1.68 and 1.91 fold, respectively.   These reduction results reveal that the activity of the photocatalysts evaluated in terms of their oxidation can not be referenced to predict their activity for reduction.   The pure TiO_2 calcined at 600 °C, which comprised of anatase and rutile phase, showed the highest oxidation efficiency for RhB, but exhibited lower activity than the sample calined at 500 °C for CO_2 reduction.   Moreover, heavy doping of V ions in the TiO_2 lattice greatly reduced the oxidative activity.   In contrast, the reductive activity of 1.00 at.% V-doped TiO_2 is similar to that of doped TiO_2 with 0.01 at.% V-ion loading.   These phenomena imply that the surface properties determine the photoreductive kinetics of the catalysts in stead of bulk microstructures.   In addition, formation of V_2O_5 moieties at high-temperatures prevents the reoxidation of CH_4.   To further explore the surface reactions, the species generated on the samples after irradiation with UV light under different atmospheres was characterized using EPR.

It is found that the color of the photocatalysts changed during the photoreductive reactions.   Figure 4-19 and 4-20 show the photographs of the photocatalysts before and after the reactions.   All the photocatalysts turned to grey after the reactions.   Interestingly, the grey color became lighter quickly when the photocatalysts stopped photocatalysis and were exposed to ambient air.   After few hours later, the color of the photocatalysts returned to their original color.   This phenomenon implies that some carbonaceous intermediates are generated and block on the photocatalysts during the CO_2 reduction.   The incompletely reduced carbons are likely soon oxidized with O_2 to become CO_2 again.   These intermediates might determine the low reduction kinetics in the photoreduction of CO_2 because of their high reduction activation barrier and occupation on the active sites.

51
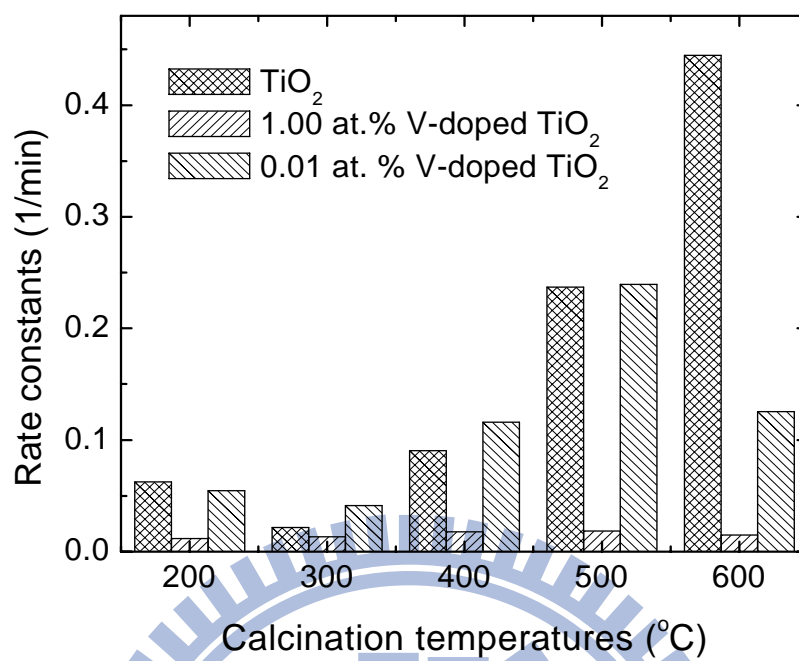
Figure 4-15 The rate constants of the pure and the V-doped TiO_2 calcined at different temperatures.
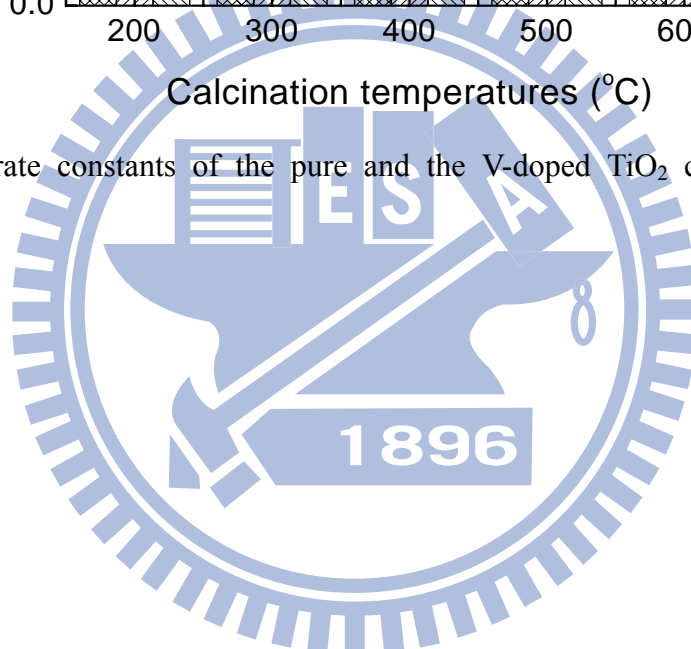
(a)
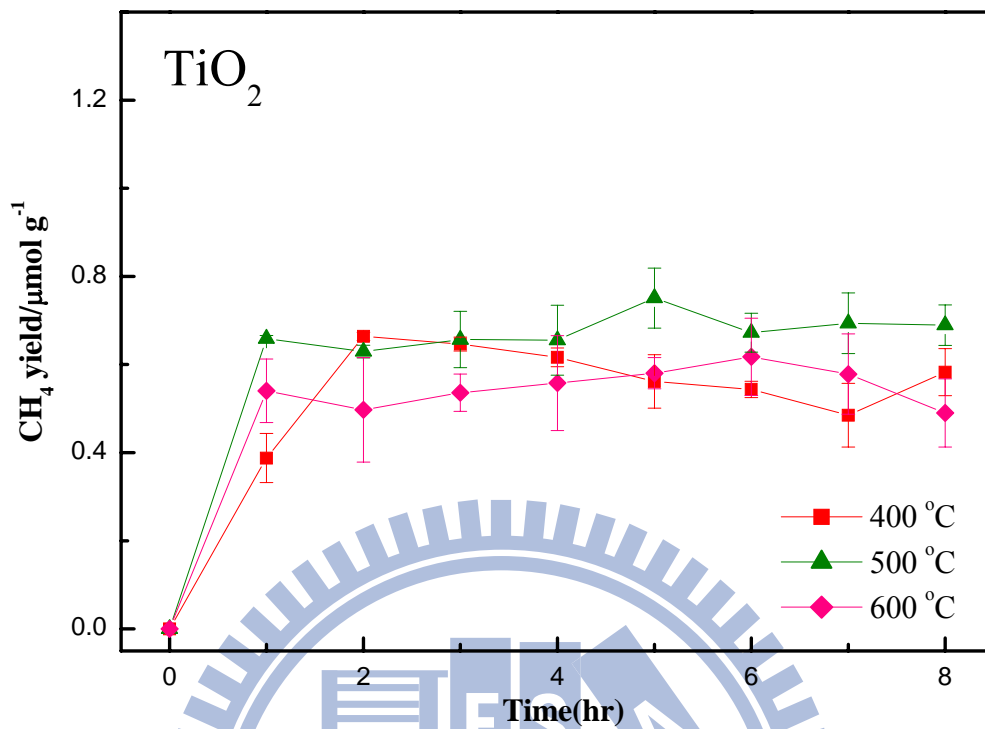
(b)
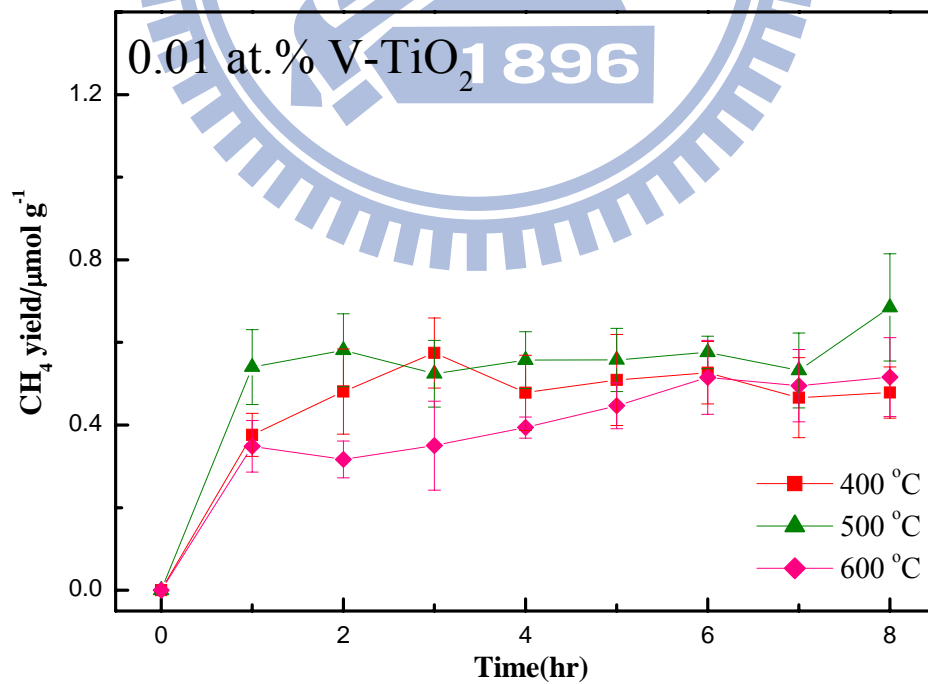
Figure 4-16 The photoreduction of CO_2 by (a) pure TiO_2 and (b) 0.01 at.% V-doped TiO_2 at 400, 500, 600 °C, respectively, to produce CH_4.
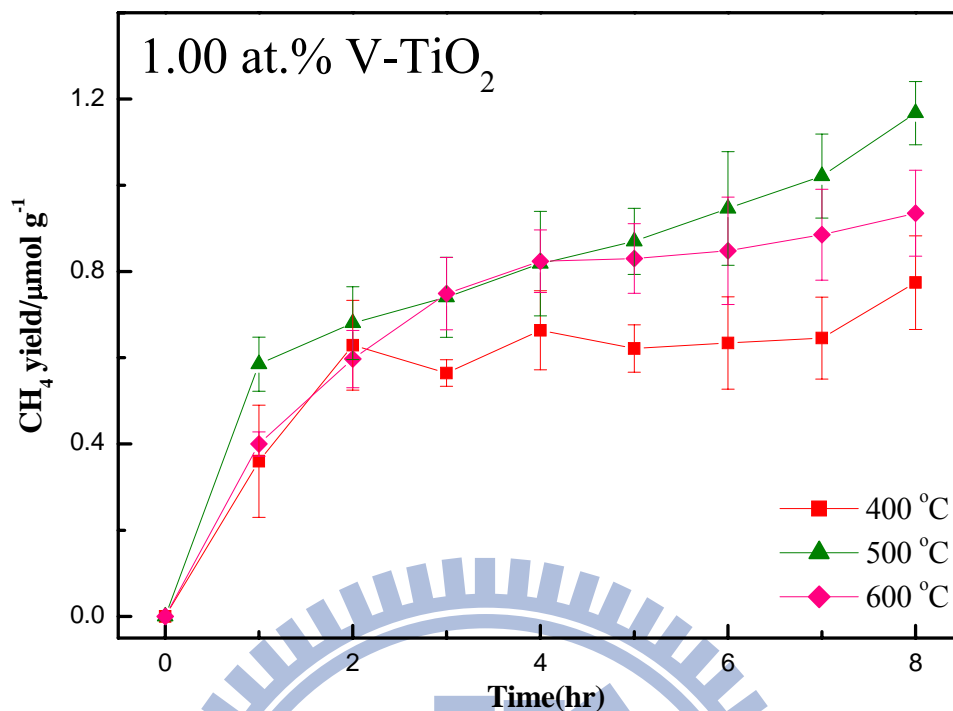
Figure 4-17 The photoreduction of CO_2 by 1.00 at.% V-doped TiO_2 at 400, 500, 600 °C, respectively, to produce CH_4.

Table 4-4 The methane yield, quantum efficiency of catalyst

Catalyst	Calcined temperature	The accumulated CH₄ yield in 1 hr (μmol/g catalyst)	QE in 1hr (%)	The accumulated CH₄ yield in 8 hr (μmol/g catalyst)	QE in 8hr (%)
Pure TiO_2	400 °C	0.39	1.75	0.58	0.33
	500 °C	0.66	2.98	0.69	0.39
	600 °C	0.54	2.44	0.49	0.28
0.01 at.% V-doped TiO_2	400 °C	0.38	1.70	0.48	0.27
	500 °C	0.54	2.44	0.68	0.39
	600 °C	0.34	1.58	0.52	0.29
1.00 at.% V-doped TiO_2	400 °C	0.36	1.63	0.77	0.44
	500 °C	0.59	2.65	1.17	0.66
	600 °C	0.40	1.81	0.94	0.53

(a)
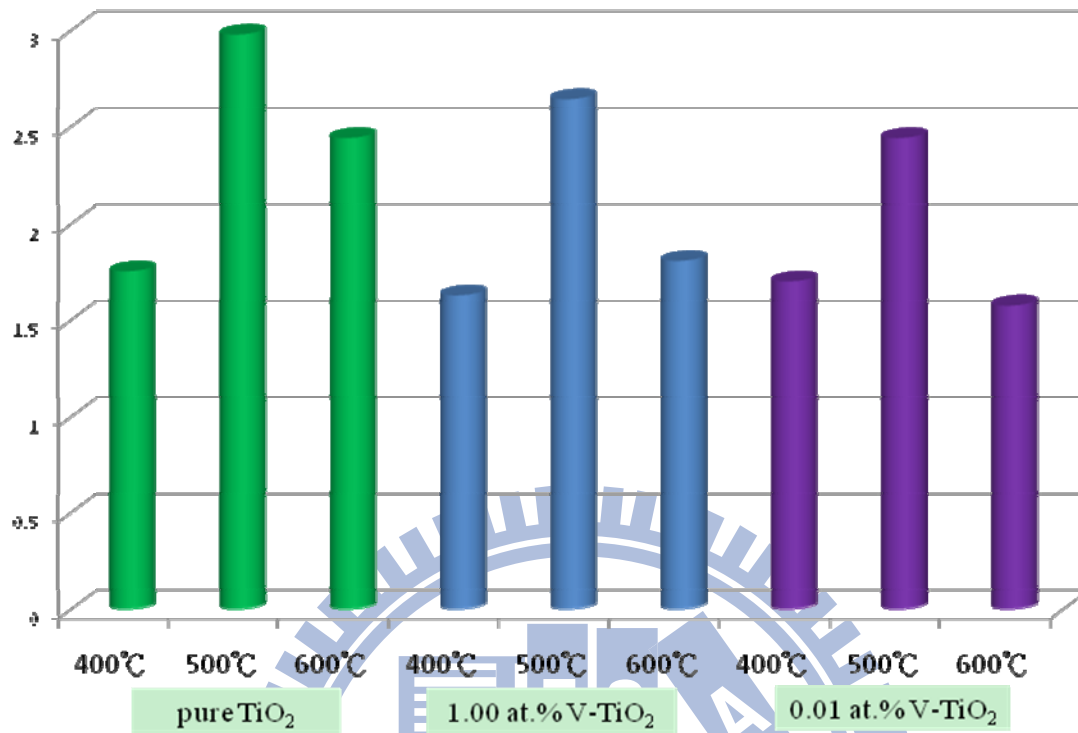
(b)
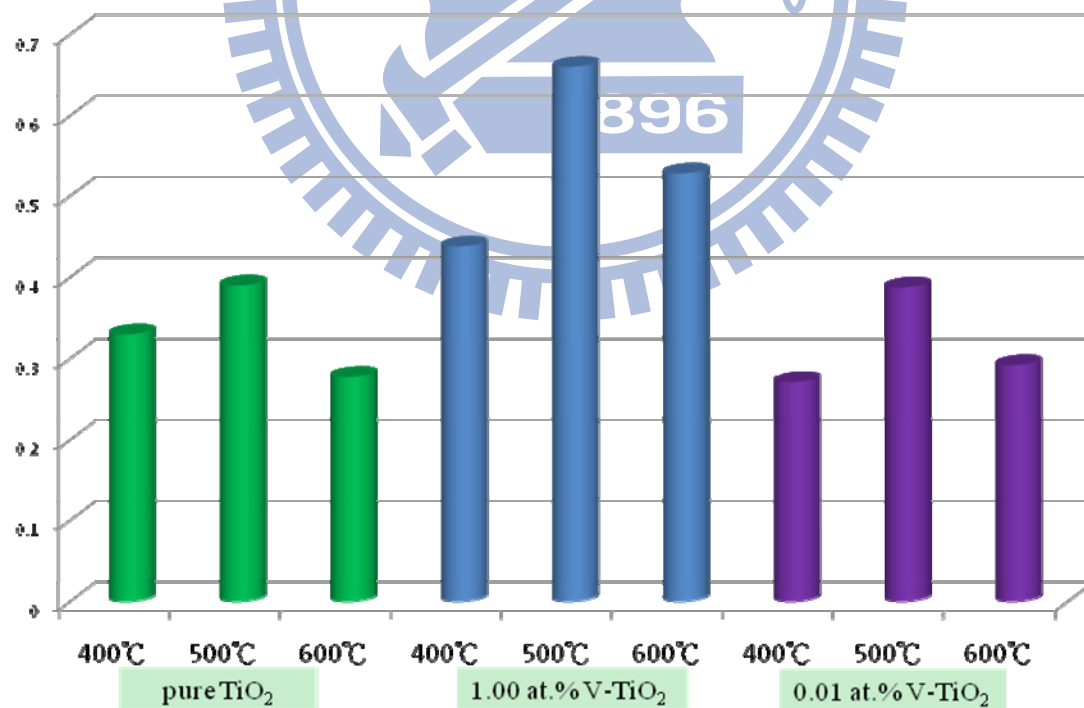
Figure 4-18 The quantum efficiency of the pure TiO_2, 1.00 and 0.01 at.% V-doped TiO_2 (a) after 1-hr irradiation and (b) after 8-hr irradiation.

Table 4-5 Some Reports on Photocatalytic Reduction of CO_2.

Light source	Catalyst	Reaction medium	Products	QE	Reference
UV lamp	Ti-SiO$_2$ film	CO_2 and H_2O vapor	methane and methanol	QE=0.28%	[86]
UV 365 nm	Ag/Cu-TiO$_2$ coated optical fiber	CO_2 and H_2O vapor	methanol	QE=0.00013%	[6]
Natural sunlight of AM 1.5 illumination	Cu, Pt cocatalyzed N-doped TiO$_2$ nanotube arrays	CO_2 and H_2O vapor	methane, other alkanes, olefins, Br-paraffins, H2, CO.	QE=0.74%	[85]
Xe arc lamp	Cu/TiO$_2$	CO_2 and H_2O vapor	CO and CH$_4$	QE=0.56%	[84]

TiO₂ at 400 °C

0.01 at.% V-TiO₂ at 400 °C

1.00 at.% V-TiO₂ at 400 °C

Figure 4-19 The pictures of pure TiO₂, 0.01 at.% V-doped TiO₂ and 1.00 at.% V-doped TiO₂ at 400 °C before and after photocalystic reaction, respectively.

Before photocatalytic reaction　　　After photocatalytic reaction
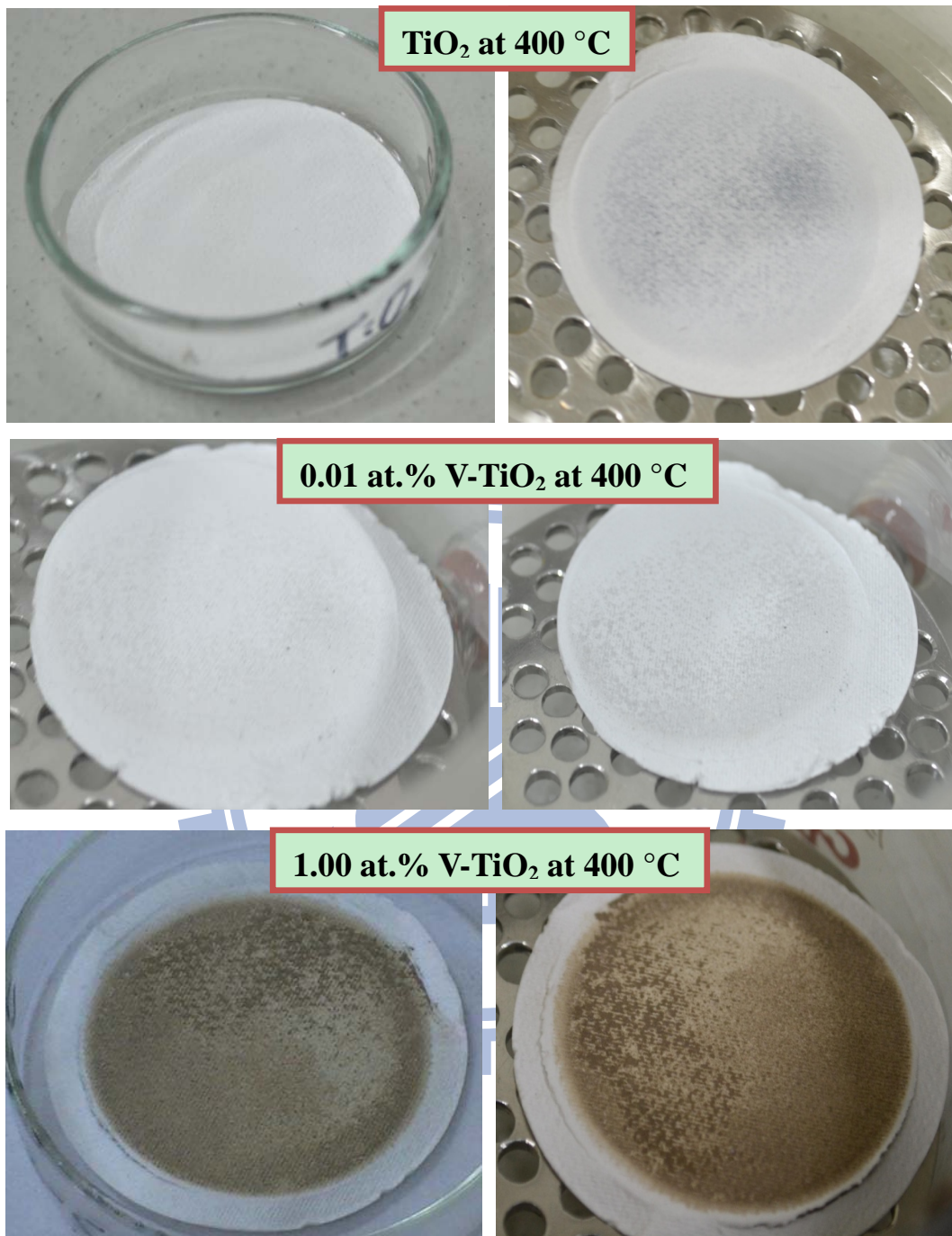
Figure 4-20 The pictures of pure TiO_2, 0.01 at.% V-doped TiO_2 and 1.00 at.% V-doped TiO_2 at 500 °C before and after photocatalystic reaction, respectively.

4-5 The discussion of photoreduction and oxidation activity

Figure 4-21 illustrates the EPR spectra of the pure TiO_2 calcined at different calcination temperatures. All the spectra were recorded after UV irradiation at 77 K. The EPR spectra of the pure TiO_2 did not show any signals in the dark (See Appendix B-1). After irradiation, the trapped holes (O^-) with g_1=2.016, g_2=2.012, g_3=2.002 were observed in the TiO_2. The signal at g=2.057 also be detected, denoting superoxide radical anion (O_2^-).[72, 87] A broad signal at g=1.9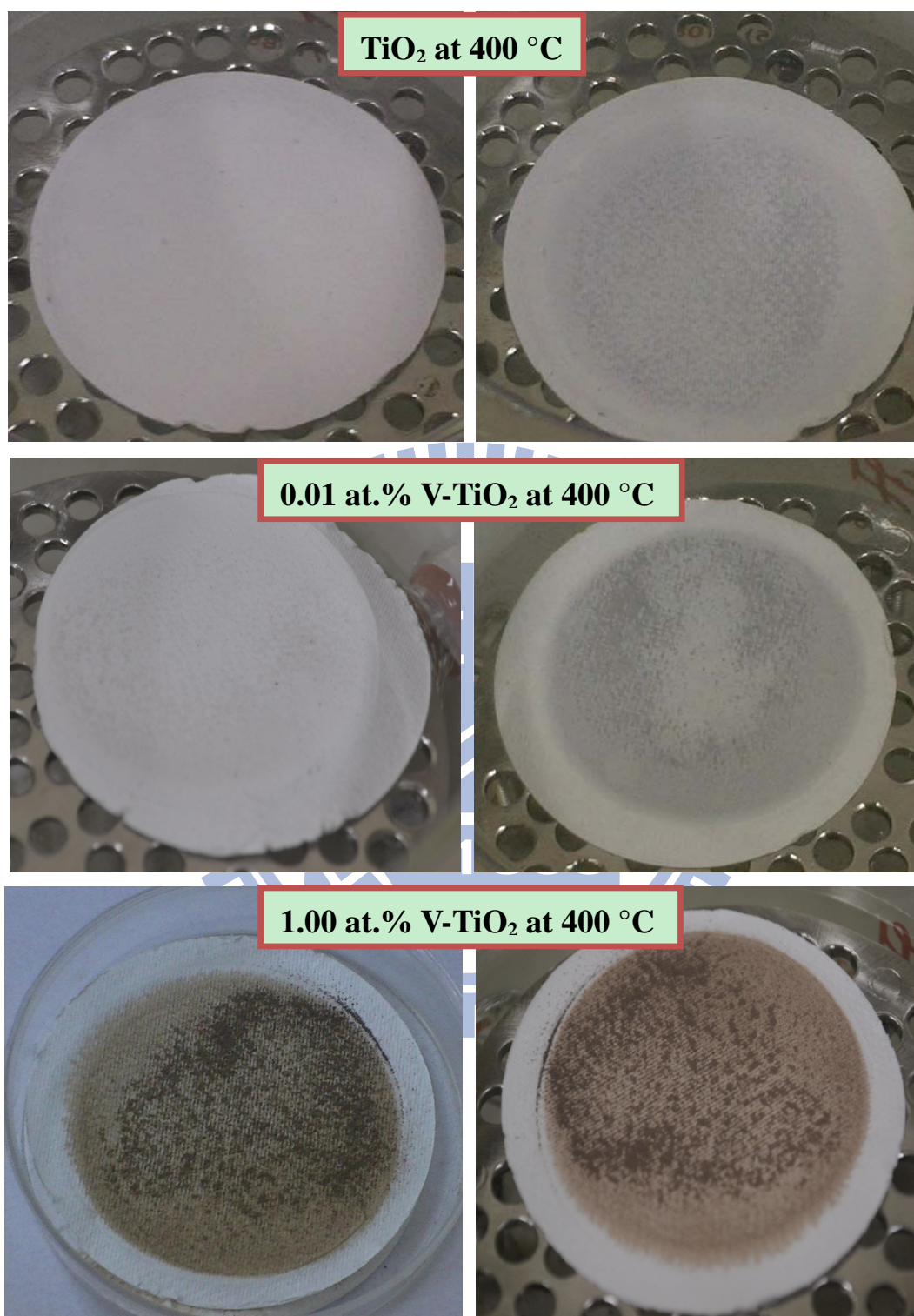65 was related to conduction electrons of Ti^{3+}.[72] Because Ti^{3+} ions are easily oxidization to Ti^{4+}, this signal is not very obvious. The signals of the trapped holes were weak in the TiO_2 sample at 200 °C. The poor crystallinity causes severe recombination and results in low quantity of surface trapped charge carriers. When the temperature increased to 300-400 °C, the intensity of the trapped holes increased with the calcination temperature. Thermal induced crystallization facilitates the charge carriers diffusing the surface. On the other hand, the increase in the crystallite sizes reduced their surface areas at elevated temperatures. Apparently, the numbers of the trapped holes in the TiO_2 sample decreased when the temperature was over 500 °C. The intensity of trapped-hole signals decreased with increasing particle sizes was also reported.[88] After normalization with surface areas, the density of surface trapped holes increased with calcination temperatures. The TiO_2 sample underwent phase transition at 600 °C. The significant increase in the trapped hole density at the surface indicates that the combination of anatse and rutile phases effectively preserves large quantity of charge carries from inhibiting bulk recombination. This contribution is due to their relative band structures which assist charge separation into the two polymorphs. Although small surface area led to fewer amounts of the trapped holes in the TiO_2 samples calcined at high temperatures, they performed superior activity for RhB degradation. This phenomenon reveals that interfacial charge transfer is efficient in these TiO_2 samples, and the microstructures dominate the

photocatalytic activity.

Figure 4-22 illustrates the EPR spectra of the 1.00 at.% and 0.01 at.% V-doped TiO_2 at different calcination temperatures. The signals of V^{4+} and trapped holes were observed. The V^{4+} signals were decreased in their intensities as the temperature increased from 200 to 500 °C. and in turn become intensive at 600 °C. At low temperatures, both the reduction and oxidation of the V^{4+} ions to V^{3+} and V^{5+} states from the dehydroxylation of the TiO_2 matrix and the exposure to ambient oxygen, respectively, reduce their numbers. At 600 °C, the great increase in the number of V^{4+} ions is presumably due to disproportionation between the V^{3+} and the V^{5+} ions. Weak trapped holes signals were observed in the 0.01 at.% V-doped TiO_2 samples. However, they were absent in the samples doped with 1.00 at.% V ions. It indicates that over amounts of defects lead to severe electron-hole recombination, thus remarkably inhibiting the photocatalytic efficiency of oxidizing RhB.

To explore the interfacial charge transfer between the photocatalysts and the CO_2, the species generated on the photocatalysts irradiated with UV light under atmospheres were examined using EPR. Prior to the measurements, all samples were heated at 120 °C to remove the surface volatile contaminants. Figure 4-23 shows the EPR spectra of the pure TiO_2 under vacuum, humidified N_2, CO_2, and humidified CO_2 atmospheres. In the vacuum, the pure TiO_2 showed the trapped holes (O⁻) with g_1=2.016, g_2=2.012, g_3=2.002. However, the signals of the trapped holes are rapidly decreased in the CO_2 atmosphere. This finding suggests that the CO_2 mediates the electrons from the conduction band to the trapped holes. In addition, it's hard to reduce CO_2 without any hole scavenger. In the presence of water vapor, the signals of the trapped holes (O⁻) were decreased due to water splitting. It is worthy to note that the trapped hole became insensitive in the humidified CO_2 atmosphere. Since the efficient charge transfer between the surface of the photocatalysts and the adsorbed CO_2 or water has been demonstrated, the intensive hole signals indicate that such interfacial transfer is limited when CO_2 and water vapor co-exists. It is possibly due to the formation

of reduced intermediates when the CO_2 molecules receive electrons and H^+ ions from the conduction band and water, respectively. Further reduction of the intermediates is inefficient, thus they occupied the surface to prevent the following interactions of CO_2 and water with the surface charge carries. The intermediates also determine the low reduction efficiency in the photocatalysis. In fact, the color charges of the catalysts during the photoreduction were observed. The surface interactions of the TiO_2 under different atmospheres are illustrated in Figure 4-24.

Figure 4-25 shows EPR spectra of the 0.01 at.% V-doped TiO_2 under different atmospheres. The effects of the atmospheres on the surface trapped radicals in the V-doped TiO_2-based systems were similar to those in the pure TiO_2-based system. However, the decrease in the intensity of the trapped holes was more obvious in the V-doped TiO_2 sample under humidified N_2 atmosphere. The p-n junction between the V_2O_5 moiety and the TiO_2 crystals drives the hole diffusion to the V_2O_5 moiety could reduce the trapped holes on the TiO_2 surface. Figure 4-26 shows the electronic structures of V_2O_5 and TiO_2 composite. The less oxidative holes in the V_2O_5 moiety inhibit re-oxidation of CH_4. The high loading of V ions in the TiO_2 results in large amounts of V_2O_5 on the surface. Therefore, the concentration of the CH_4 product constantly increased in the presence of the 1.00 at.% V-doped TiO_2 sample. On the other hand, the high density of surface defects introduces substantial energy states below the conduction band. Electrons trapped at these less reductive states are considered to cause the doped TiO_2 samples exhibiting lower initial activity than the pure TiO_2 photocatalyst.

(a)
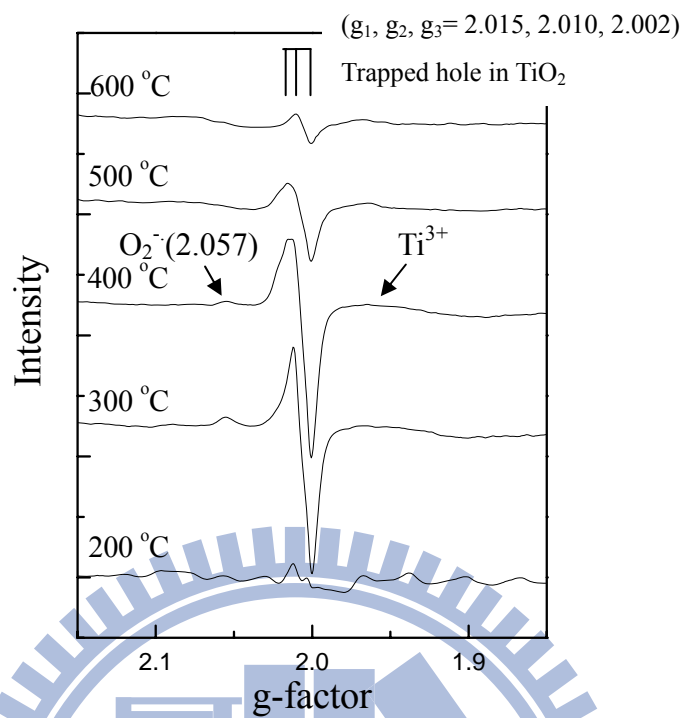
(b)
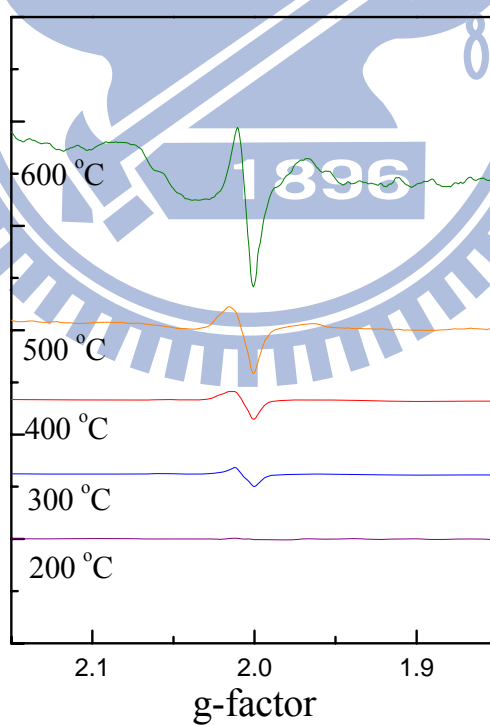
Figure 4-21 EPR spectra of the pure TiO_2 at different calcination temperature at 77K under UV irradiation.   (a) Raw data and (b) the data normalized with surface areas.

(a)
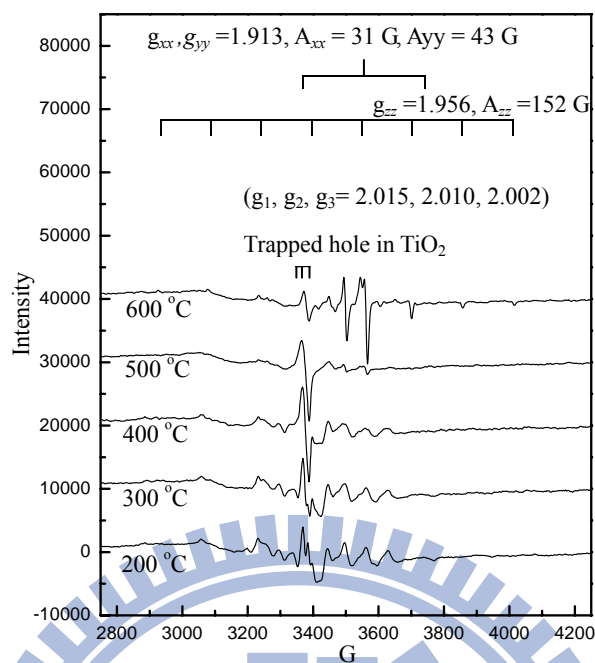
(b)
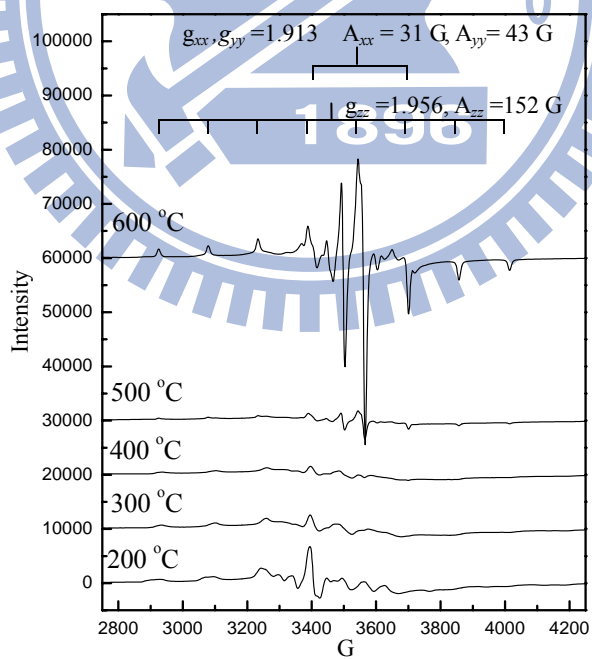
Figure 4-22. EPR spectra of the (a) 1.00 at.% V-doped TiO_2 and (b) the 0.01 at.% V-doped TiO_2 calcained at different temperatures.   All the spectra were recorded at 77 K under UV irradiation.
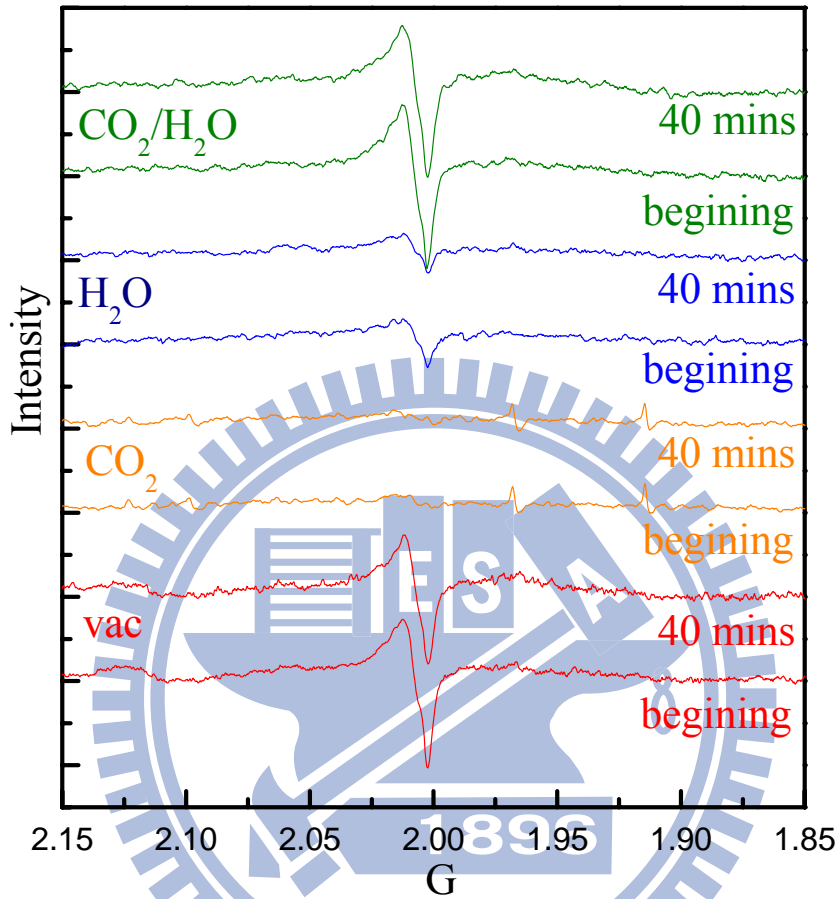
Figure 4-23 EPR spectra of the pure TiO_2 at different atmosphere conditions. The data recorded when the UV irradiated in the beginning and after 40 mins irradiation.
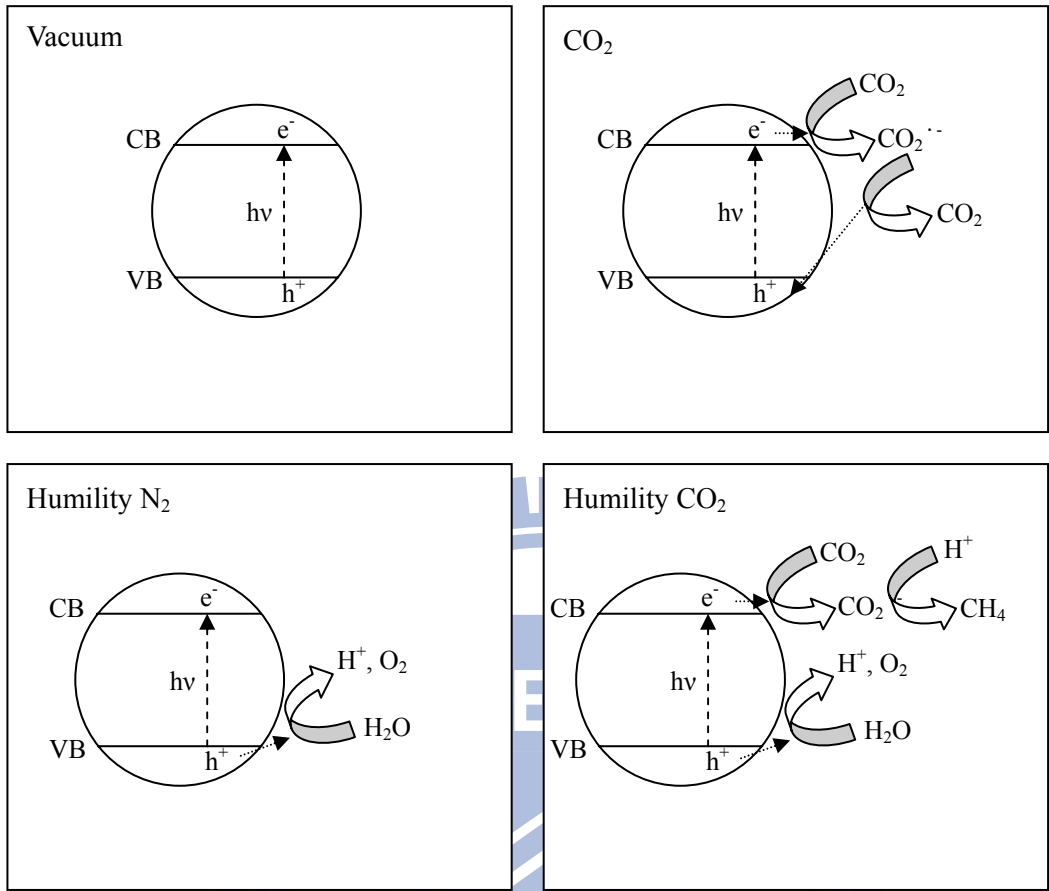
Figure 4-24 The concept of photocatalytic reaction of different atmosphere.
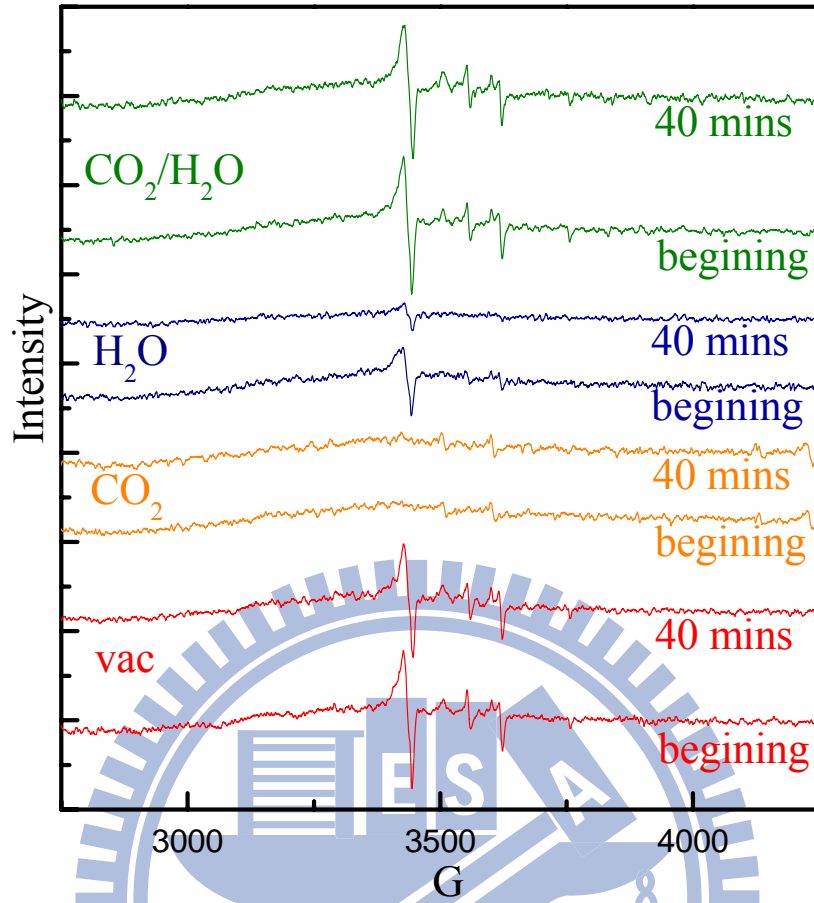
Figure 4-25 EPR spectra of the 0.01 at.% V-doped TiO_2 at different atmosphere conditions. The data recorded when the UV irradiated in the beginning and after 40 mins irradiation.
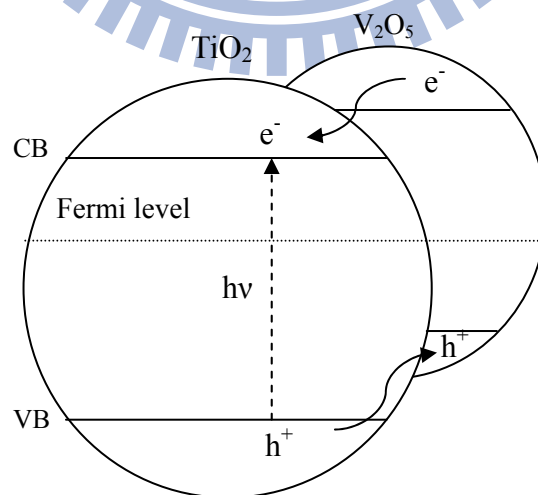
Figure 4-26 The electronic structures of V_2O_5 at the surface of TiO_2.[35]

Chapter 5. Conclusions

In this study, the doped V ions migrated from the bulk lattice to the TiO_2 surface above 300 °C, thus increasing their surface concentration by 7.6 times as the temperature increased to 600 °C. The concentrated V ions at the surface induce V_2O_5 crystals formed in the TiO_2 surface region. The incorporation of V ions into the TiO_2 lattice accelerated the phase transformation and resulted in a lower phase transit temperature of 500 °C. The bandgap energy of the TiO_2 was greatly reduced from 3.1-3.3 eV to 1.6 eV when 1.00 at.% V ions are doped. The photocatalytic activity of the TiO_2 samples for RhB degradation increased with calcination temperatures because of improved crystallinity. Doping trace amounts of V ions enhanced the oxidative activity. However, high concentrations of V ions in the bulk lattice induced severe charge recombination and reduce numbers of effective charge carriers. The pure TiO_2 calcined at 600 °C, which comprised of anatase and rutile phase, showed the highest oxidation efficiency for RhB. However, the TiO_2 sample calined at 500 °C exhibited the highest activity for CO_2 reduction. The high concentrations of V-doped TiO_2 increased the yield of CH_4 with increased calcination temperature and reached the highest yield of CH_4 at 500 °C. Methane yield by high concentrations of V-doped TiO_2 was 1.68 times higher than the pure TiO_2. The QE of CH_4 was reached to 0.66%. However, the initial yield of CH_4 was 0.89 times lower than the pure TiO_2. This study showed that the V^{3+} and V^{4+} ions in the bulk of TiO_2 suppress the ability of the electron transfer efficiency because V^{3+} and V^{4+} ions acted as recombination centers. However, V_2O_5, formed by increasing calcination temperature, on TiO_2 was helpful to preserve methane from reoxidation because it decreased the ability of oxidation of TiO_2. The formation of reduced intermediates was observed to occupy the surface to prevent the following interactions of CO_2 and water with the surface charge carries.

References

1.   Roy, S.C., O.K. Varghese, M. Paulose, and C.A. Grimes, *Toward Solar Fuels: Photocatalytic Conversion of Carbon Dioxide to Hydrocarbons.* Acs Nano, 2010. **4**(3): p. 1259-1278.

2.   Di Paola, A., E. Garcia-Lopez, S. Ikeda, G. Marci, B. Ohtani, and L. Palmisano, *Photocatalytic degradation of organic compounds in aqueous systems by transition metal doped polycrystalline TiO2.* Catalysis Today, 2002. **75**(1-4): p. 87-93.

3.   Klosek, S. and D. Raftery, *Visible light driven V-doped TiO2 photocatalyst and its photooxidation of ethanol.* Journal of Physical Chemistry B, 2001. **105**(14): p. 2815-2819.

4.   Kemp, T.J. and R.A. McIntyre, *Transition metal-doped titanium(IV) dioxide: Characterisation and influence on photodegradation of poly(vinyl chloride).* Polymer Degradation and Stability, 2006. **91**(1): p. 165-194.

5.   Bouras, P., E. Stathatos, and P. Lianos, *Pure versus metal-ion-doped nanocrystalline titania for photocatalysis.* Applied Catalysis B-Environmental, 2007. **73**(1-2): p. 51-59.

6.   Wu, J.C.S., T.H. Wu, T.C. Chu, H.J. Huang, and D.P. Tsai, *Application of optical-fiber photoreactor for CO2 photocatalytic reduction.* Topics in Catalysis, 2008. **47**(3-4): p. 131-136.

7.   Wang, C.J., R.L. Thompson, J. Baltrus, and C. Matranga, *Visible Light Photoreduction of CO2 Using CdSe/Pt/TiO2 Heterostructured Catalysts.* Journal of Physical Chemistry Letters, 2010. **1**(1): p. 48-53.

8.   Adachi, K., K. Ohta, and T. Mizuno, *Photocatalytic Reduction of Carbon-Dioxide to Hydrocarbon Using Copper-Loaded Titanium-Dioxide.* Solar Energy, 1994. **53**(2): p. 187-190.

9.   Choi, W.Y., A. Termin, and M.R. Hoffmann, *The Role of Metal-Ion Dopants in Quantum-Sized TiO2 - Correlation between Photoreactivity and Charge-Carrier Recombination Dynamics.* Journal of Physical Chemistry, 1994. **98**(51): p. 13669-13679.

10.   Wachs, I.E., Y. Chen, J.M. Jehng, L.E. Briand, and T. Tanaka, *Molecular structure and reactivity of the Group V metal oxides.* Catalysis Today, 2003. **78**(1-4): p. 13-24.

11.   Bronkema, J.L., D.C. Leo, and A.T. Bell, *Mechanistic studies of methanol oxidation to formaldehyde on isolated vanadate sites supported on high surface area anatase.* Journal of Physical Chemistry C, 2007. **111**(39): p. 14530-14540.

12.   Diebold, U., *The surface science of titanium dioxide.* Surface Science Reports, 2003. **48**(5-8): p. 53-229.

13.   Schwarzburg, K. and F. Willig, *Diffusion impedance and space charge capacitance in*

the nanoporous dye-sensitized electrochemical solar cell. Journal of Physical Chemistry B, 2003. **107**(15): p. 3552-3555.

14. Sclafani, A. and J.M. Herrmann, *Comparison of the photoelectronic and photocatalytic activities of various anatase and rutile forms of titania in pure liquid organic phases and in aqueous solutions.* Journal of Physical Chemistry, 1996. **100**(32): p. 13655-13661.

15. Skubal, L.R., N.K. Meshkov, and M.C. Vogt, *Detection and identification of gaseous organics using a TiO2 sensor.* Journal of Photochemistry and Photobiology a-Chemistry, 2002. **148**(1-3): p. 103-108.

16. Usubharatana, P., D. McMartin, A. Veawab, and P. Tontiwachwuthikul, *Photocatalytic process for CO2 emission reduction from industrial flue gas streams.* Industrial & Engineering Chemistry Research, 2006. **45**(8): p. 2558-2568.

17. Linsebigler, A.L., G.Q. Lu, and J.T. Yates, *Photocatalysis on TiO2 Surfaces - Principles, Mechanisms, and Selected Results.* Chemical Reviews, 1995. **95**(3): p. 735-758.

18. Kabra, K., R. Chaudhary, and R.L. Sawhney, *Treatment of hazardous organic and inorganic compounds through aqueous-phase photocatalysis: A review.* Industrial & Engineering Chemistry Research, 2004. **43**(24): p. 7683-7696.

19. Wold, A., *Photocatalytic Properties of TiO2.* Chemistry of Materials, 1993. **5**(3): p. 280-283.

20. Litter, M.I., *Heterogeneous photocatalysis - Transition metal ions in photocatalytic systems.* Applied Catalysis B-Environmental, 1999. **23**(2-3): p. 89-114.

21. Anpo, M. and M. Takeuchi, *The design and development of highly reactive titanium oxide photocatalysts operating under visible light irradiation.* Journal of Catalysis, 2003. **216**(1-2): p. 505-516.

22. Herrmann, J.M., *Heterogeneous photocatalysis: fundamentals and applications to the removal of various types of aqueous pollutants.* Catalysis Today, 1999. **53**(1): p. 115-129.

23. Reddy, K.M., B. Baruwati, M. Jayalakshmi, M.M. Rao, and S.V. Manorama, *S-, N- and C-doped titanium dioxide nanoparticles: Synthesis, characterization and redox charge transfer study.* Journal of Solid State Chemistry, 2005. **178**(11): p. 3352-3358.

24. Wang, H. and J.P. Lewis, *Second-generation photocatalytic materials: anion-doped TiO2.* Journal of Physics-Condensed Matter, 2006. **18**(2): p. 421-434.

25. Zhao, G.L., H. Kozuka, H. Lin, and T. Yoko, *Sol-gel preparation of Ti1-xVxO2 solid solution film electrodes with conspicuous photoresponse in the visible region.* Thin Solid Films, 1999. **339**(1-2): p. 123-128.

26. Wu, J.C.S. and C.H. Chen, *A visible-light response vanadium-doped titania nanocatalyst by sol-gel method.* Journal of Photochemistry and Photobiology

a-Chemistry, 2004. **163**(3): p. 509-515.

27. Anpo, M., S. Dohshi, M. Kitano, Y. Hu, M. Takeuchi, and M. Matsuoka, *The preparation and characterization of highly efficient titanium oxide-based photofunctional materials.* Annual Review of Materials Research, 2005. **35**: p. 1-27.

28. Fujishima, A. and K. Honda, *Electrochemical Photolysis of Water at a Semiconductor Electrode.* Nature, 1972. **238**(37-38).

29. Davidson, A. and M. Che, *Temperature-Induced Diffusion of Probe Vanadium(Iv) Ions into the Matrix of Titanium-Dioxide as Investigated by Esr Techniques.* Journal of Physical Chemistry, 1992. **96**(24): p. 9909-9915.

30. Rodella, C.B., P.A.P. Nascente, V.R. Mastelaro, M.R. Zucchi, R.W.A. Franco, C.J. Magon, P. Donoso, and A.O. Florentino, *Chemical and structural characterization of V2O5/TiO2 catalysts.* Journal of Vacuum Science & Technology A, 2001. **19**(4): p. 1158-1163.

31. Zhao, G.L., G.R. Han, M. Takahashi, and T. Yoko, *Photoelectrochemical properties of sol-gel-derived Ti1-xVxO2 solid solution film photoelectrodes.* Thin Solid Films, 2002. **410**(1-2): p. 14-20.

32. Izumi, Y., K. Konishi, T. Miyajima, and H. Yoshitake, *Photo-oxidation over mesoporous V-TiO2 catalyst under visible light monitored by vanadium K beta(5,2)-selecting XANES spectroscopy.* Materials Letters, 2008. **62**(6-7): p. 861-864.

33. Xu, J.J., Y.H. Ao, M.D. Chen, D.G. Fu, and C.W. Yuan, *Photocatalytic activity of vanadium-doped titania-activated carbon composite film under visible light.* Thin Solid Films, 2010. **518**(15): p. 4170-4174.

34. Hoffmann, M.R., J. Choi, and H. Park, *Combinatorial doping of TiO(2) with platinum (Pt), chromium (Cr), vanadium (V), and nickel (Ni) to achieve enhanced photocatalytic activity with visible light irradiation.* Journal of Materials Research, 2010. **25**(1): p. 149-158.

35. Chang, S.-m. and W.-s. Liu, *Surface doping is more beneficial than bulk doping to the photocatalytic activity of vanadium-doped TiO2.* Applied Catalysis B: Environmental, 2011. **101**: p. 333-342.

36. Alyea, E.C., L.J. Lakshmi, and Z. Ju, *Spectroscopic and activity studies on vanadia supported on titania and phosphorus-modified titania.* Langmuir, 1997. **13**(21): p. 5621-5626.

37. Izumi, Y., F. Kiyotaki, N. Yagi, A.M. Vlaicu, A. Nisawa, S. Fukushima, H. Yoshitake, and Y. Iwasawa, *X-ray absorption fine structure combined with X-ray fluorescence spectrometry. Part 15. Monitoring of vanadium site transformations on Titania and in mesoporous titania by selective detection of the vanadium K alpha(1) fluorescence.* Journal of Physical Chemistry B, 2005. **109**(31): p. 14884-14891.

38. Wachs, I.E., J.M. Jehng, and W. Ueda, *Determination of the chemical nature of active*

surface sites present on bulk mixed metal oxide catalysts. Journal of Physical Chemistry B, 2005. **109**(6): p. 2275-2284.

39.   Bulushev, D.A., L. Kiwi-Minsker, V.I. Zaikovskii, and A. Renken, *Formation of active sites for selective toluene oxidation during catalyst synthesis via solid-state reaction of V2O5 with TiO2.* Journal of Catalysis, 2000. **193**(1): p. 145-153.

40.   Hansen, J.E., *Scientific reticence and sea level rise.* Environmental Research Letters, 2007. **2**(2): p. -.

41.   Chisti, Y., *Biodiesel from microalgae.* Biotechnology Advances, 2007. **25**(3): p. 294-306.

42.   Galvez, M.E., P.G. Loutzenhiser, I. Hischier, and A. Steinfeld, *CO2 splitting via two-step solar thermochemical cycles with Zn/ZnO and FeO/Fe3O4 redox reactions: Thermodynamic analysis.* Energy & Fuels, 2008. **22**(5): p. 3544-3550.

43.   Bamberger, C.E. and P.R. Robinson, *Thermochemical Splitting of Water and Carbon-Dioxide with Cerium Compounds.* Inorganica Chimica Acta-Articles, 1980. **42**(1): p. 133-137.

44.   Inoue, T., A. Fujishima, S. Konishi, and K. Honda, *Photoelectrocatalytic Reduction of Carbon-Dioxide in Aqueous Suspensions of Semiconductor Powders.* Nature, 1979. **277**(5698): p. 637-638.

45.   Halmann, M., *Photoelectrochemical Reduction of Aqueous Carbon-Dioxide on P-Type Gallium-Phosphide in Liquid Junction Solar-Cells.* Nature, 1978. **275**(5676): p. 115-116.

46.   Anpo, M., H. Yamashita, Y. Ichihashi, and S. Ehara, *Photocatalytic Reduction of CO2 with H2O on Various Titanium-Oxide Catalysts.* Journal of Electroanalytical Chemistry, 1995. **396**(1-2): p. 21-26.

47.   Sayama, K. and H. Arakawa, *Photocatalytic Decomposition of Water and Photocatalytic Reduction of Carbon-Dioxide over ZrO2 Catalyst.* Journal of Physical Chemistry, 1993. **97**(3): p. 531-533.

48.   Lo, C.C., C.H. Hung, C.S. Yuan, and J.F. Wu, *Photoreduction of carbon dioxide with H-2 and H2O over TiO2 and ZrO2 in a circulated photocatalytic reactor.* Solar Energy Materials and Solar Cells, 2007. **91**(19): p. 1765-1774.

49.   Halmann, M., M. Ulman, and B. Aurianblajeni, *Photochemical Solar Collector for the Photoassisted Reduction of Aqueous Carbon-Dioxide.* Solar Energy, 1983. **31**(4): p. 429-431.

50.   Tseng, I.H., W.C. Chang, and J.C.S. Wu, *Photoreduction of CO2 using sol-gel derived titania and titania-supported copper catalysts.* Applied Catalysis B-Environmental, 2002. **37**(1): p. 37-48.

51.   Mizuno, T., K. Adachi, K. Ohta, and A. Saji, *Effect of CO2 pressure on photocatalytic reduction of CO2 using TiO2 in aqueous solutions.* Journal of Photochemistry and

Photobiology a-Chemistry, 1996. **98**(1-2): p. 87-90.

52. Lacombe, S., H. Cardy, N. Soggiu, S. Blanc, J.L. Habib-Jiwan, and J.P. Soumillion, *Diffuse reflectance UV-Visible spectroscopy for the qualitative and quantitative study of chromophores adsorbed or grafted on silica.* Microporous and Mesoporous Materials, 2001. **46**(2-3): p. 311-325.

53. Uvarov, V. and I. Popov, *Metrological characterization of X-ray diffraction methods for determination of crystallite size in nano-scale materials.* Materials Characterization, 2007. **58**(10): p. 883-891.

54. Surnev, S., M.G. Ramsey, and F.P. Netzer, *Vanadium oxide surface studies.* Progress in Surface Science, 2003. **73**(4-8): p. 117-165.

55. Yamashita, H., Y. Ichihashi, M. Takeuchi, S. Kishiguchi, and M. Anpo, *Characterization of metal ion-implanted titanium oxide photocatalysts operating under visible light irradiation.* Journal of Synchrotron Radiation, 1999. **6**: p. 451-452.

56. Silversmit, G., J.A. van Bokhoven, H. Poelman, A.M.J. van der Eerden, G.B. Marin, M.F. Reyniers, and R. De Gryse, *The structure of supported and unsupported vanadium oxide under calcination, reduction and oxidation determined with XAS.* Applied Catalysis a-General, 2005. **285**(1-2): p. 151-162.

57. Bordage, A., E. Balan, J.P.R. de Villiers, R. Cromarty, A. Juhin, C. Carvallo, G. Calas, P.V.S. Raju, and P. Glatzel, *V oxidation state in Fe-Ti oxides by high-energy resolution fluorescence-detected X-ray absorption spectroscopy.* Physics and Chemistry of Minerals, 2011. **38**(6): p. 449-458.

58. J. Wong, F.W.L., R. P. Messmer and D. H. Maylotte, *K-edge absorption spectra of selected vanadium compounds.* Physical review B, 1984. **30**(10): p. 5596-5611.

59. Izumi, Y., K. Konishi, D.M. Obaid, T. Miyajima, and H. Yoshitake, *X-ray absorption fine structure combined with X-ray fluorescence spectroscopy. Monitoring of vanadium sites in mesoporous titania, excited under visible light by selective detection of vanadium K beta(5,2) Fluorescence.* Analytical Chemistry, 2007. **79**(18): p. 6933-6940.

60. Silversmit, G., H. Poelman, I. Sack, G. Buyle, G.B. Marin, and R. De Gryse, *An in-situ reduction/oxidation XAS study on the EL10V8 VOx/TiO2(Anatase) powder catalyst.* Catalysis Letters, 2006. **107**(1-2): p. 61-71.

61. Frank, P., E.J. Carlson, R.M.K. Carlson, B. Hedman, and K.O. Hodgson, *The uptake and fate of vanadyl ion in ascidian blood cells and a detailed hypothesis for the mechanism and location of biological vanadium reduction. A visible and X-ray absorption spectroscopic study.* Journal of Inorganic Biochemistry, 2008. **102**(4): p. 809-823.

62. Rodella, C.B. and V.R. Mastelaro, *Structural characterization of the V2O5/TiO2 system obtained by the sol-gel method.* Journal of Physics and Chemistry of Solids,

2003. **64**(5): p. 833-839.

63. Balikdjian, J.P., A. Davidson, S. Launay, H. Eckert, and M. Che, *Sintering and phase transformation of V-loaded anatase materials containing bulk and surface V species.* Journal of Physical Chemistry B, 2000. **104**(38): p. 8931-8939.

64. Bentrup, U., A. Bruckner, C. Rudinger, and H.J. Eberle, *Elucidating structure and function of active sites in VOx/TiO2 catalysts during oxyhydrative scission of 1-butene by in situ and operando spectroscopy.* Applied Catalysis a-General, 2004. **269**(1-2): p. 237-248.

65. Li, C.Z., B.Z. Tian, F. Gu, H.B. Jiang, Y.J. Hu, and J.L. Zhang, *Flame sprayed V-doped TiO(2) nanoparticles with enhanced photocatalytic activity under visible light irradiation.* Chemical Engineering Journal, 2009. **151**(1-3): p. 220-227.

66. Gratzel, M. and R.F. Howe, *Electron-Paramagnetic Resonance Studies of Doped Tio2 Colloids.* Journal of Physical Chemistry, 1990. **94**(6): p. 2566-2572.

67. Chary, K.V.R., G. Kishan, T. Bhaskar, and H. Sivaraj, *Structure and reactivity of vanadium oxide catalysts supported on anatase TiO2.* Journal of Physical Chemistry B, 1998. **102**(35): p. 6792-6798.

68. Howe, R.F. and M. Gratzel, *Electron-Paramagnetic-Res Study of Hydrated Anatase under Uv Irradiation.* Journal of Physical Chemistry, 1987. **91**(14): p. 3906-3909.

69. Nakaoka, Y. and Y. Nosaka, *ESR Investigation into the effects of heat treatment and crystal structure on radicals produced over irradiated TiO2 powder.* Journal of Photochemistry and Photobiology a-Chemistry, 1997. **110**(3): p. 299-305.

70. Hurum, D.C., K.A. Gray, T. Rajh, and M.C. Thurnauer, *Recombination pathways in the Degussa P25 formulation of TiO2: Surface versus lattice mechanisms (vol 109B, pg 980, 2005).* Journal of Physical Chemistry B, 2005. **109**(11): p. 5388-5388.

71. Kumar, C.P., N.O. Gopal, T.C. Wang, M.S. Wong, and S.C. Ke, *EPR investigation of TiO2 nanoparticles with temperature-dependent properties.* Journal of Physical Chemistry B, 2006. **110**(11): p. 5223-5229.

72. Coronado, J.M., A.J. Maira, J.C. Conesa, K.L. Yeung, V. Augugliaro, and J. Soria, *EPR study of the surface characteristics of nanostructured TiO2 under UV irradiation.* Langmuir, 2001. **17**(17): p. 5368-5374.

73. Martin, S.T., C.L. Morrison, and M.R. Hoffmann, *Photochemical Mechanism of Size-Quantized Vanadium-Doped TiO2 Particles.* Journal of Physical Chemistry, 1994. **98**(51): p. 13695-13704.

74. Hibino, M., M. Ugaji, A. Kishimoto, and T. Kudo, *Preparation and Lithium Intercalation of a New Vanadium-Oxide with a 2-Dimensional Structure.* Solid State Ionics, 1995. **79**: p. 239-244.

75. Oliveri, G., G. Ramis, G. Busca, and V.S. Escribano, *Thermal-Stability of Vanadia-Titania Catalysts.* Journal of Materials Chemistry, 1993. **3**(12): p. 1239-1249.

76. del Val, S., M.L. Granados, J.L.G. Fierro, J. Santamaria-Gonzalez, A.J. Lopez, and T. Blasco, *alpha-TiP-supported vanadium oxide catalysts: Influence of calcination pretreatments on structure and performance for o-xylene oxidation*. Journal of Catalysis, 2001. **204**(2): p. 466-478.

77. Amores, J.M.G., V.S. Escribano, and G. Busca, *Anatase Crystal-Growth and Phase-Transformation to Rutile in High-Area TiO2, MoO3-TiO2 and Other Tio2-Supported Oxide Catalytic-Systems*. Journal of Materials Chemistry, 1995. **5**(8): p. 1245-1249.

78. Balikdjian, J.P., A. Davidson, S. Launay, H. Eckert, and M. Che, *Sintering and phase transformation of V-loaded anatase materials containing bulk and surface species (vol 104B, pg 8931, pg 2000)*. Journal of Physical Chemistry B, 2001. **105**(49): p. 12432-12432.

79. Choi, J., H. Park, and M.R. Hoffmann, *Effects of Single Metal-Ion Doping on the Visible-Light Photoreactivity of TiO2*. Journal of Physical Chemistry C, 2010. **114**(2): p. 783-792.

80. Luan, Z.H. and L. Kevan, *Electron spin resonance and diffuse reflectance ultraviolet-visible spectroscopies of vanadium immobilized at surface titanium centers of titanosilicate mesoporous TiMCM-41 molecular sieves*. Journal of Physical Chemistry B, 1997. **101**(11): p. 2020-2027.

81. Zheng, S., L. Gao, Q.H. Zhang, W.P. Zhang, and J.K. Guo, *Preparation, characterization and photocatalytic properties of singly and doubly titania-modified mesoporous silicate MCM-41 by varying titanium precursors*. Journal of Materials Chemistry, 2001. **11**(2): p. 578-583.

82. Li, Y., T.J. White, and S.H. Lim, *Low-temperature synthesis and microstructural control of titania nano-particles*. Journal of Solid State Chemistry, 2004. **177**(4-5): p. 1372-1381.

83. Yu, J.G., H.G. Yu, B. Cheng, X.J. Zhao, J.C. Yu, and W.K. Ho, *The effect of calcination temperature on the surface microstructure and photocatalytic activity of TiO2 thin films prepared by liquid phase deposition*. Journal of Physical Chemistry B, 2003. **107**(50): p. 13871-13879.

84. Li, Y., W.N. Wang, Z.L. Zhan, M.H. Woo, C.Y. Wu, and P. Biswas, *Photocatalytic reduction of CO2 with H2O on mesoporous silica supported Cu/TiO2 catalysts*. Applied Catalysis B-Environmental, 2010. **100**(1-2): p. 386-392.

85. Varghese, O.K., M. Paulose, T.J. LaTempa, and C.A. Grimes, *High-Rate Solar Photocatalytic Conversion of CO2 and Water Vapor to Hydrocarbon Fuels*. Nano Letters, 2009. **9**(2): p. 731-737.

86. Ikeue, K., S. Nozaki, M. Ogawa, and M. Anpo, *Photocatalytic reduction of CO2 with H2O on Ti-containing porous silica thin film photocatalysts*. Catalysis Letters, 2002.

80(3-4): p. 111-114.

87. Coronado, J.M., A.J. Maira, A. Martinez-Arias, J.C. Conesa, and J. Soria, *EPR study of the radicals formed upon UV irradiation of ceria-based photocatalysts.* Journal of Photochemistry and Photobiology a-Chemistry, 2002. **150**(1-3): p. 213-221.

88. Manivannan, A., G. Glaspell, and P. Dutta, *Synthesis of nanocrystalline TiO2 particles and their structural characteristics.* Journal of Cluster Science, 2008. **19**(2): p. 391-399.
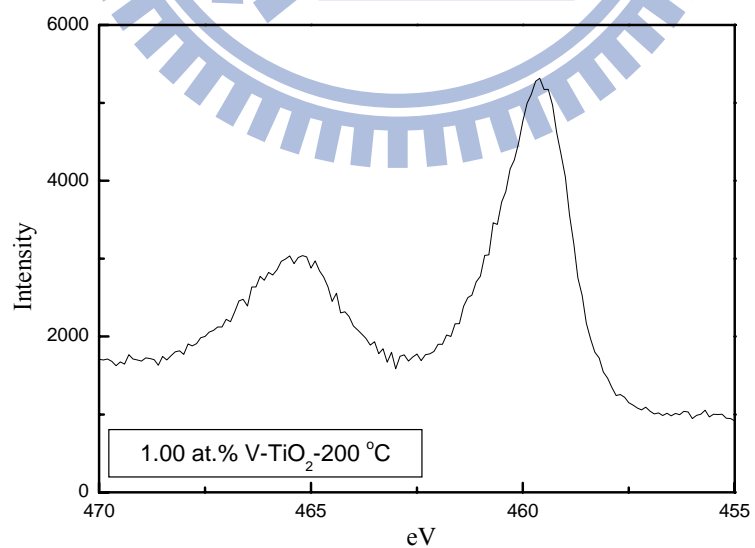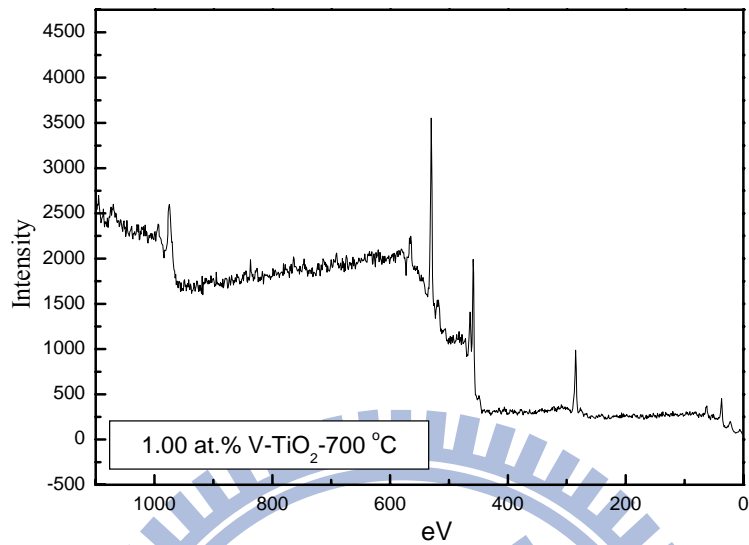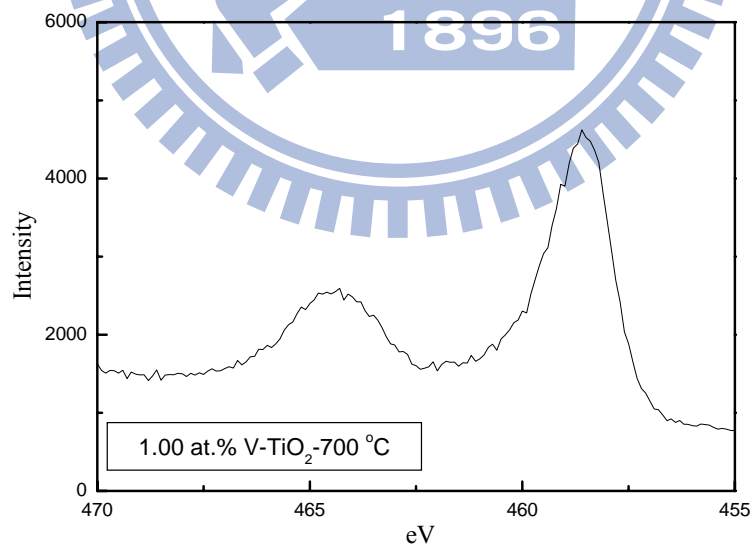
Appendix A. XPS Analysis

(a)
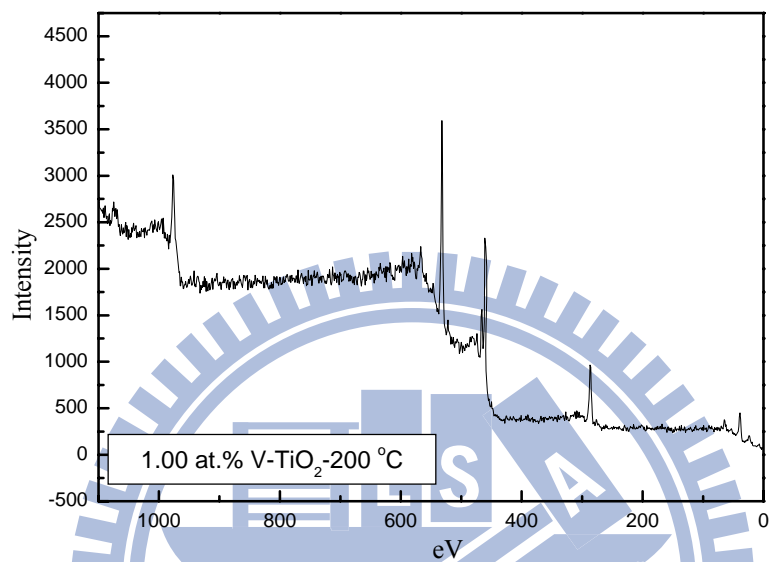
(b)

Appendix A-1 The XPS spectra of the 1.00 at.% V-doped TiO_2 at 200 °C. (a) survey and (b) Ti (2p).

(a)

(b)

Appendix A-2 The XPS spectra of the 1.00 at.% V-doped TiO_2 at 700 °C. (a) survey and (b) Ti (2p).

(a)
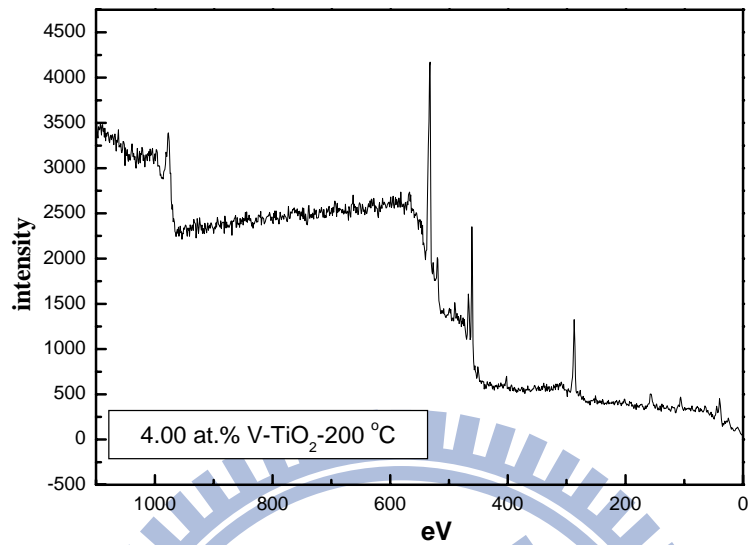
(b)
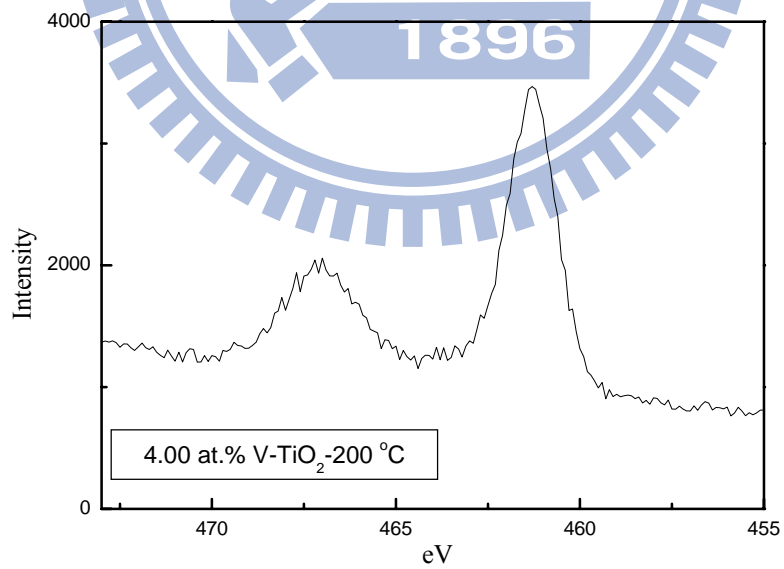
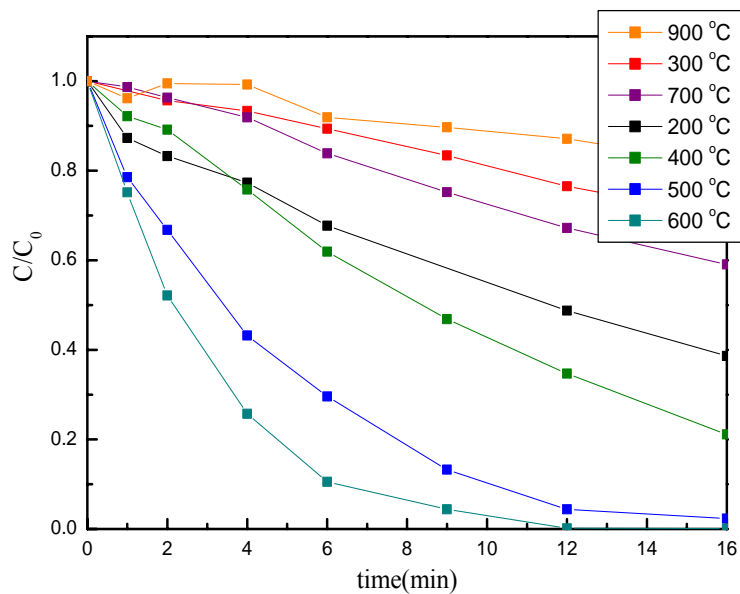Appendix A-3 The XPS spectra of the 4.00 at.% V-doped TiO_2 at 200 °C. (a) survey and (b) Ti (2p).
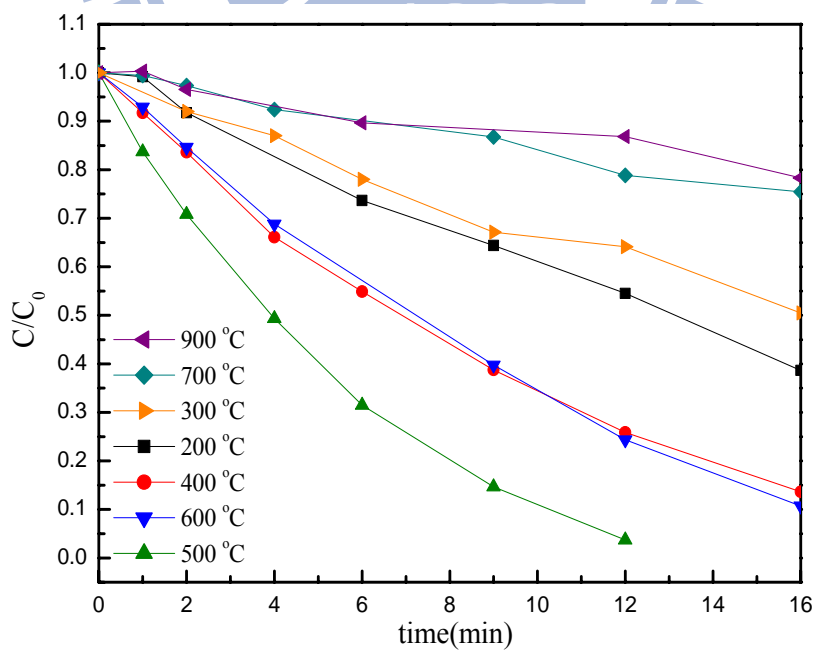
Appendix B. EPR Analysis
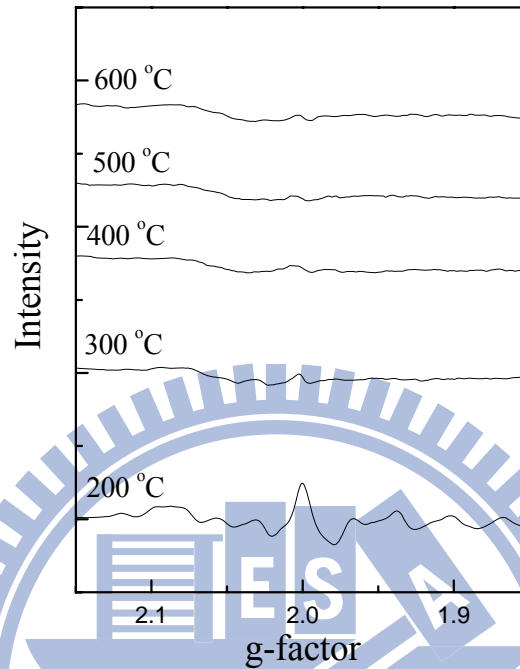
Appendix B-1 EPR spectra of pure TiO_2 at different calcination temperature at 77K in the dark.
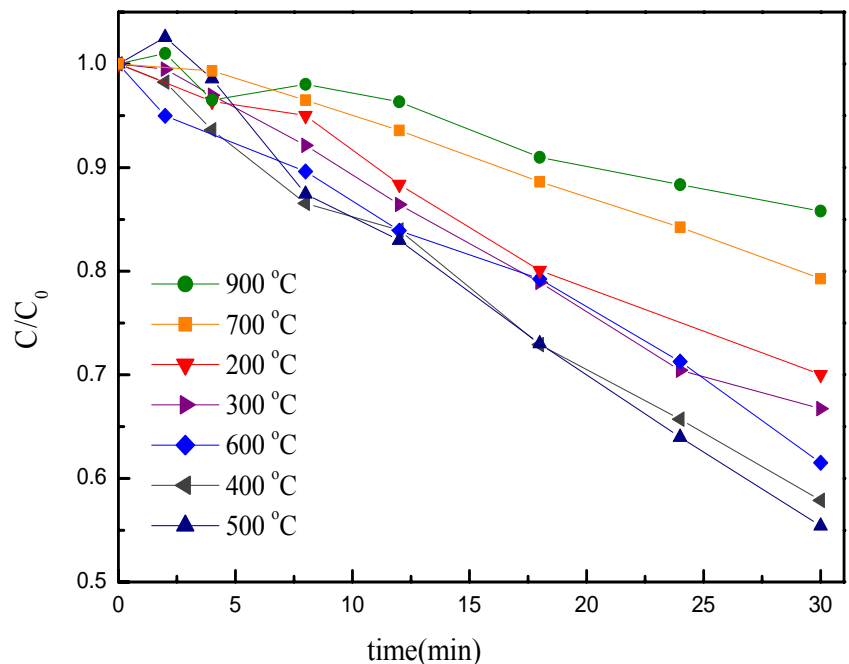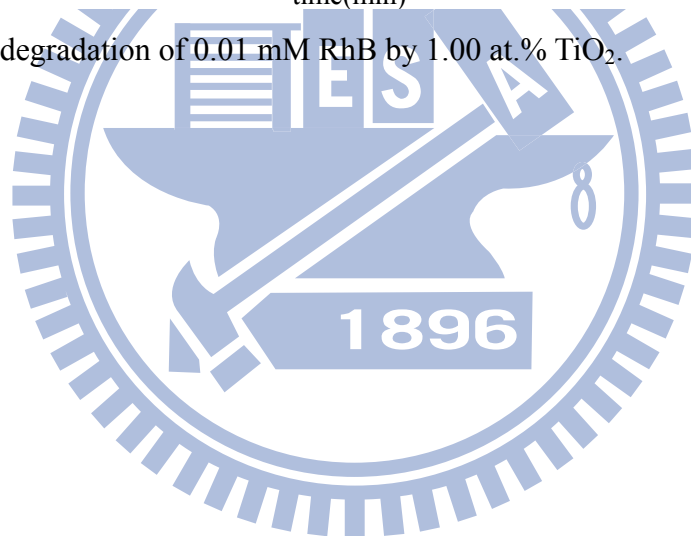
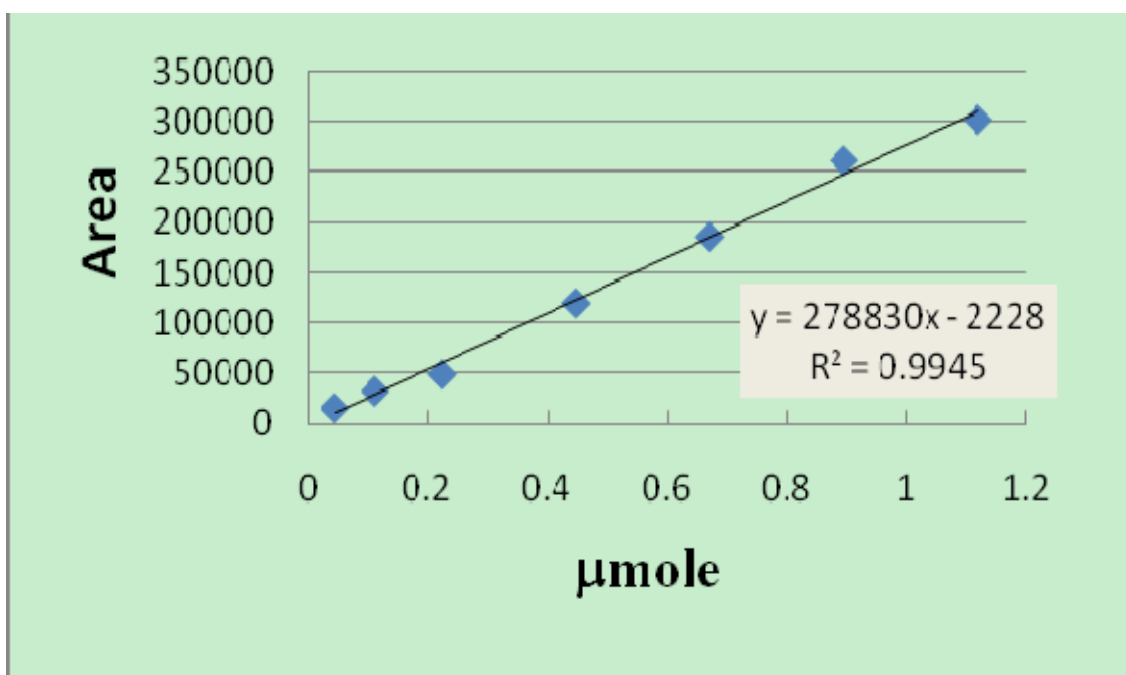# Appendix C. Degradation of RhB

(a)

(b)

Appendix C-1 The degradation of 0.01 mM RhB by (a)the pure TiO_2 and (b)the 0.01 at.% TiO_2.

Appendix C-2 The degradation of 0.01 mM RhB by 1.00 at.% TiO_2.

Appendix D. Calibration Curve

Appendix D-1 The calibration curve of CH_4.